Virus Research 149 (2010) 211–216

Contents lists available at ScienceDirect

Virus Research

journal homepage: www.elsevier.com/locate/virusres

G to A hypermutation of TT virus

Masataka Tsuge[a,b,c], Chiemi Noguchi[a,c], Rie Akiyama[a,c], Miyuki Matsushita[a,c], Kana Kunihiro[a,c], Sachi Tanaka[a,c], Hiromi Abe[a,c], Fukiko Mitsui[a,c], Shosuke Kitamura[a,c], Tsuyoshi Hatakeyama[a,c], Takashi Kimura[a,c], Daiki Miki[a,c], Nobuhiko Hiraga[a,c], Michio Imamura[a,c], Shoichi Takahashi[a,c], C. Nelson Hayses[a,c], Kazuaki Chayama[a,c,*]

[a] Department of Medicine and Molecular Science, Division of Frontier Medical Science, Programs for Biomedical Research, Graduate School of Biomedical Sciences, Hiroshima University, Hiroshima, Japan
[b] Natural Science Center for Basic Research and Development, Hiroshima University, Hiroshima, Japan
[c] Liver Research Project Center, Hiroshima University, Hiroshima, Japan

ARTICLE INFO

Article history:
Received 11 November 2009
Received in revised form 29 January 2010
Accepted 29 January 2010
Available online 6 February 2010

Keywords:
TTV
HBV
Hypermutation
APOBEC
3D-PCR

ABSTRACT

APOBEC3 proteins function as part of innate antiviral immunity and induce G to A hypermutation in retroviruses and hepatitis B virus (HBV) genomes. Whether APOBEC3 proteins affect viruses that replicate without a reverse transcription step is unknown. TT virus (TTV), known to present in serum of healthy individuals and HBV carriers, has a single-stranded circular DNA genome and replicates without reverse transcription. In this study, we examined 67 blood samples obtained from healthy individuals and HBV carriers and observed G to A hypermutation of genomes of TTV in both healthy individuals and HBV carriers. During ALT flare-up in HBV carriers, G to A hypermutation of HBV increased, but TTV genomes significantly decreased in number and hypermutated TTV genomes became undetectable. Our results show that hypermutated TTV exist in healthy individuals and HBV carriers and that TTV genomes were susceptible to immune reaction directed to HBV by interacting with APOBEC3 proteins.

1. Introduction

Apolipoprotein B editing component 3 (APOBEC3) proteins are cystidine deaminases with strong antiviral activity and act as part of antiviral innate immunity against retroviruses such as human immunodeficiency virus, simian immunodeficiency virus, equine infectious anemia virus, murine leukemia virus and foamy viruses (Delebecque et al., 2006; Harris et al., 2003; Lochelt et al., 2005; Mangeat et al., 2003; Mariani et al., 2003; Russell et al., 2005). The APOBEC enzymes induce G to A hypermutation in nascent minus-strand viral DNA, although the effect of the induction of hypermutation on the antiviral effect is not fully understood (Conticello et al., 2007). The APOBEC3 proteins are reported also to suppress the replication of hepatitis B virus (HBV) (Suspene et al., 2005a), which replicates through reverse transcription of the over length pre-genome RNA (Ganem, 2001). We and others reported the presence of hypermutated HBV genomes in serum samples of patients with chronic HBV infection (Bonvin et al., 2006; Noguchi et al., 2005, 2007; Suspene et al., 2005a).

The antiviral effects of APOBEC3 proteins are not limited to the virus that replicates through reverse transcription. H. Chen et al. (2006) showed that APOBEC3A protein inhibits the replication of adeno-associated virus, a single-stranded DNA virus. However, they did not describe the presence or absence of hypermutated genomes, hence the actual interaction between the virus and the protein remains unknown. It is thus expected that analysis of the effect of APOBEC3 proteins on other viruses and examination of hypermutated genomes may clarify the mechanisms of action of these proteins as antiviral agents (Bishop et al., 2004; Bonvin et al., 2006; Lecossier et al., 2003; Mangeat et al., 2003; Mariani et al., 2003; Noguchi et al., 2005, 2007; Rosler et al., 2005; Suspene et al., 2004; Zhang et al., 2003).

The TT virus (TTV) is a small non-enveloped single-stranded DNA virus that was first isolated from a blood sample of a patient who developed post-transfusion non-A to -G hepatitis (Nishizawa et al., 1997). TTV persistently infects healthy individuals and patients with chronic HBV infection, without affecting the clinicopathological course of chronic hepatitis B (Kao et al., 2000). The virus is a member of the genus *Alphatorquevirus* in the family *Anelloviridae* and has some similarity to chicken anemia virus.

Abbreviations: HBV, hepatitis B virus; TTV, TT virus; APOBEC3, apolipoprotein B editing component 3; IFN, interferon.

* Corresponding author at: Department of Medical and Molecular Science, Division of Frontier Medical Science, Programs for Biomedical Research, Graduate School of Biomedical Science, Hiroshima University, 1-2-3 Kasumi, Minami-ku, Hiroshima 734-8551, Japan. Tel.: +81 82 257 5190; fax: +81 82 255 6220.
E-mail address: chayama@hiroshima-u.ac.jp (K. Chayama).

0168-1702/$ – see front matter © 2010 Elsevier B.V. All rights reserved.
doi:10.1016/j.virusres.2010.01.019

Table 1
Primers used for detection of TTV and HBV genomes.

Quantitative analysis by real-time polymerase chain reaction	
TTV	
Forward primer #1	5′-CGTCACTAACCACGTGCGWYYCACA-3′ (nt: 3–27)
Reverse primer #2	5′-GCYATTYGGAAGTGCASTYAYTTATAT-3′ (nt: 78–104)
HBV	
Forward primer #3	5′-TTTGGGCATGGACATTGAC-3′ (nt: 1893–1912)
Reverse primer #4	5′-GGTGAACAATGTTCCGGAGAC-3′ (nt: 2029–2049)
Amplification and analysis of hypermutated TTV genomes by 3D-PCR	
1stPCR	
Forward primer #5	5′-CAACCRTRKRCTATGTCGTSCACTTCCT-3′ (nt: 31–58)
Reverse primer #6	5′-ATTGCYYYTTGACTKCGGTGTGTAA-3′ (nt: 184–208)
2ndPCR	
Forward primer #7	5′-ATATAARTRASTGCACTTCCRAATRGC-3′ (nt: 78–104)
Reverse primer #8	5′-ATTGCYYYTTGACTKCGGTGTGTAA-3′ (nt: 184–208)

TTV has a single-stranded circular DNA genome of approximately 3.8 kb (Hino, 2002). The replication mechanism of TTV is poorly understood because there is neither a culture system nor an animal model to support viral multiplication. Decreases in serum levels of TTV have been reported in individuals who received vaccination against influenza virus and HBV (Maggi et al., 2005), suggesting that TTV is easily targeted by the host immune system.

The present study was designed to detect hypermutated TTV genomes and search for fluctuations in the viral load during exacerbation of chronic hepatitis B to determine whether the TTV virus is also a target of APOBEC3 proteins.

2. Materials and methods

2.1. Subjects

The study population consisted of 31 healthy volunteers (mean age 34.3 ± 5.1, ±SD, male:female = 24:7) and 36 patients with chronic HBV infection who were negative for hepatitis C virus and HIV-1 markers (age 36.3 ± 11.5, male:female = 23:13, 24 tested positive for HBeAg). All subjects provided written informed consent for the donation and evaluation of blood samples. The experimental protocol was confirmed to meet the ethical guidelines of the 1975 Declaration of Helsinki and was also approved by the Hiroshima University Ethical Committee.

2.2. Extraction and quantification of TTV and HBV genomes

TTV DNA and HBV DNA were extracted from 100 μl serum obtained from the control and chronic HBV carriers using the SMITEST R&D kit, as described in the product manual (Genome Science Laboratories, Tokyo). The DNAs were dissolved separately in 20 μl H_2O. TTV and HBV genomes were quantified by real-time PCR using the 7300 Real-Time PCR System (Applied Biosystems, Foster City, CA). Amplification was performed in a 25 μl reaction mixture containing 12.5 μl SYBR Green PCR Master Mix (Applied Biosystems), 5 pmol of forward primer, 5 pmol of reverse primer, and 1 μl of DNA solution. The primers are listed in Table 1, and the nucleotide positions refer to TTV sequence AB064607. The primers were designed based on conserved regions within the reported sequences to exclude the effect of variation among the different TTV genotypes. After incubation for 2 min at 50 °C, the sample was denatured for 10 min at 95 °C, followed by a PCR cycling program consisting of 40 cycles of 15 s at 95 °C, 30 s at 55 °C and 60 s at 60 °C. The lower detection limits of both TTV and HBV quantitative assays were 10^3 copies/ml.

2.3. Amplification and sequence analysis of hypermutated TTV genomes by 3D-PCR

To find hypermutated TTV genomes, a modified 3D-PCR was used. Because the hypermutated TTV genomes contained high AT content which melts at a lower temperature than DNA with a higher GC content, we could detect AT-rich hypermutated TTV genomes by modulating the PCR denaturation temperature. The first PCR was performed in a 25 μl reaction mixture, consisting of 100 mM Tris–HCl [pH 8.3], 50 mM KCl, 15 mM $MgCl_2$, 0.2 mM each of dNTPs, 548 copies of DNA solution, 10 pmol each of primers #5 and #6, and 1.25 units of Taq DNA polymerase (Gene Taq, Wako Pure Chemicals, Tokyo), together with 0.25 μg anti-Taq high (Toyobo Co., Osaka, Japan). The amplification conditions included initial denaturation at 95 °C for 5 min, followed by 45 cycles of denaturation at 95 °C for 1 min, annealing at 50 °C for 30 s, extension at 72 °C for 1 min, followed by 10 min of final extension at 72 °C. Hypermutated genomes were detected by modified 3D-PCR (differential DNA denaturation PCR) using 1 μl of the first PCR product as input in 25 μl of 100 mM Tris–HCl [pH 8.3], 50 mM KCl, 15 mM $MgCl_2$, 0.2 mM each of dNTPs, 10 pmol of primers #7 and #6, and 1.25 unit of Taq DNA polymerase together with 0.25 μg anti-Taq high. Primers #5, #6 and #7 are also described in Table 1. The amplification conditions included initial denaturation at 79–95 °C for 5 min, followed by 35 cycles of denaturation at 79–95 °C for 1 min, annealing at 50 °C for 30 s, extension at 72 °C for 30 s followed by 10 min of final extension. Amplicons were separated by electrophoresis on 2% (w/v) agarose gel, cloned and sequenced in the ABI PLISM3130 Genetic analyzer (Applied Biosystems) with Big Dye Terminator Version 3.1 Cycle Sequencing Ready Reaction kit (Applied Biosystems). The second-round 3D-PCR yielded a 131 bp fragment. To confirm that amplified products were indeed hypermutated and not a PCR artifact, the 3D-PCR products were also electrophoresed in agarose gels containing Hanse Analytik (HA) yellow, which is a pegylated bisbenzamide that interacts preferentially with the minor groove of AT-rich DNA, thus retarding migration (Noguchi et al., 2007; Suspene et al., 2005b). The detection limit of hypermutated genomes was 10^3 copies/ml.

2.4. Quantitative analysis of HBV hypermutated genomes by TaqMan PCR

Hypermutated HBV genomes were quantified by TaqMan PCR using the 7300 Real-Time PCR System (Applied Biosystems). The primers used for amplification were as follows: forward primer 5′-ACTTCAACCCCAACAMRRATCA-3′ (nt: 2978–2999), reverse primer 5′-AGAGYTTGKTGGAATGTKGTGGA-3′ (nt: 24–1), where M is A/C, R is G/A, Y is T/C, and K is G/T (nucleotide numbers are those of HBV genotype C as reported by Norder et al., 1994). The probe was 6-carboxyfluorescein (FAM)-labeled MGB probe, 5′-(FAM)-TTAGAGGTGGAGAGATGG-(MGB)-3′ (nt: 3184–3167). The amplification conditions included activation at 95 °C for 10 min followed by initial denaturation at 88 °C for 20 min and 45 cycles of amplification (denaturation at 88 °C for 15 s, annealing at 50 °C for 30 s, and extension at 62 °C for 90 s). 88 °C as denaturation temperature was appropriate for detection of about 20% hypermutated genomes. The buffer comprised 10 mM Tris–HCl [pH 8.3], 50 mM KCl, 3 mM $MgCl_2$, 10 mM ethylenediaminetetraacetic acid (EDTA), 60 nM Passive Reference 1, 0.2 mM each of dNTPs, 0.9 μM each of primers, 0.25 μM of probe, 5×10^6 copies of HBV DNA, and 0.625 unit of AmpliTaq Gold DNA polymerase (Applied Biosystems) in a final volume of 25 μl. A standard curve was constructed by simultaneously amplifying serial dilutions of the 3D-PCR products. The detection limit of hypermutated genomes was 10^2 copies/ml.

Table 2
Background of healthy individuals and HBV carriers.

	Control subjects (n = 31)	HBV carriers (n = 36)
Age (mean ± SD)	34.3 ± 5.1	36.3 ± 11.5
Gender (male:female)	24:7	23:13
TTV DNA [log copies/ml]	3.96[a] (<2.00–5.11)	4.15[a] (<2.00–6.07)
HBV marker		
HBeAg:HBeAb		28:7
HBVDNA [LGEAml]		7.8[a] (3.6 to >8.8)
Liver function		
T. bilirubin [mg/dl]	ND	0.8[a] (0.3–20.0)
ALT [IU/l]	ND	72[a] (10–1150)
Albumin [mg/dl]	ND	4.4[a] (2.3–5.4)

ND: not determined.
[a] Median value.

3. Results

3.1. Detection and quantification of serum TTV and HBV DNAs

Real-time PCR was used for screening of TTV DNA and HBV DNA. TTV DNA was detected in 22 of 31 (71.0%) healthy individuals and in 29 of 36 (80.6%) HBV carriers. The clinical profiles of these individuals are shown in Table 2. The median TTV DNA titers (and range) in healthy individuals and HBV carriers were 3.96 log copies/ml (<2.00–5.11) and 4.95 log copies/ml (<2.00–6.07), respectively. The median HBV DNA titer (and range) in the patients was 7.8 (3.6 to >8.8) log genome equiv./ml.

3.2. Screening for hypermutated TTV genomes in normal subjects and HBV carriers

We selected the four subjects with the highest TTV titers from each group and collected adequate sample volumes from the control and HBV carriers listed in Table 2 for further analysis. The clinical data of these eight individuals are shown in Fig. 1a. We screened for hypermutated TTV genomes using modified 3D-PCR and HA yellow gel electrophoresis. The lower the denaturation temperature of the 3D-PCR assay the smaller the number of positive samples detected (Fig. 1b). Detection of hypermutated genomes by 3D-PCR was confirmed by HA yellow gel electrophoresis in all cases. A typical representation is shown in Fig. 1b. The amplified hypermutated genomes were cloned and nucleotide sequences determined. Hypermutated TTV genomes were detected in both HBV carriers and healthy individuals (Fig. 1c).

3.3. Sequence analysis of hypermutated TTV genomes

To analyze the frequency of G to A hypermutation, we determined the consensus sequence of the TTV genomes by direct sequencing using the PCR products amplified using a denaturation temperature of 90 °C and compared the sequences between the consensus sequence and the sequences obtained from eight clones by cloning and sequencing PCR products at lower denaturation temperatures. The frequencies of hypermutation were as follow: 81 °C – 54.5–61.4% (mean: 57.8%), 83 °C – 52.3–59.1% (mean: 56.3%), 85 °C – 29.5–59.1% (mean: 51.1%), 88 °C – 9.1–56.8% (mean: 20.6%) and 90 °C – 4.5–34.1% (mean: 11.0%).

3.4. Context of G to A hypermutation

To see the actual hypermutation sequences, we performed sequence analysis of the 3D-PCR products at the lowest denaturation temperature (Fig. 1b, B3, 81 °C). We found extensive G to A mutations in these clones (Fig. 2a and b), with as many as 21 out of 30 G residues (70%) being replaced by A. We used the HyperPack software package (Kijak et al., 2007) to analyze the incidence of G to A hypermutations and their context in the nucleotide sequence.

The nucleotides positioned 1 or 2 bases 5′ of G residues did not affect the frequency of G to A mutation (Fig. 2c and d). In contrast, a significantly higher rate of G to A substitution was observed in G residues in a GA or GG context ($P < 0.001$, chi-square test or Fisher's exact test) (Fig. 2e).

3.5. Flare-up of ALT in HBV carriers is associated with falls in TTV DNA titer

We reported recently that the level of hypermutation in HBV genomes increases during exacerbation of chronic hepatitis (Noguchi et al., 2009). Next, we searched for possible increases in hypermutation in both HBV and TTV genomes during flare-ups of hepatitis in HBV carriers. Interestingly, while the level of hypermutated HBV genomes increased during flare-ups, TTV titers decreased significantly, and the occurrence of hypermutated TTV genomes became undetectable (Fig. 3).

4. Discussion

There is a general agreement that APOBEC3 proteins are part of innate immunity and induce G to A hypermutation in viruses that replicate via reverse transcription. In contrast, there are no concrete data on whether these proteins interact with and inhibit replication of viruses that replicate without reverse transcription. To date, only one study has reported the presence of a TTV genome with multiple G to A substitutions (Ball et al., 1999). The authors identified only a single hypermutated TTV genome among 93 sequences examined, but they did not report the nucleotide sequence. Consequently, the degree or context of hypermutation is unknown.

In this study, we found hypermutated TTV genomes in healthy individuals as well as HBV carriers using the 3D-PCR method. We also analyzed the context of G to A substitutions and found that a significantly higher rate of G to A substitution was observed in G residues in a GA or GG context ($P < 0.001$, chi-square test or Fisher's exact test) (Fig. 2e). In contrast, the nucleotides positioned 1 or 2 bases 5′ of G residues did not affect the frequency of G to A mutation (Fig. 2c and d). According to previous reports, hypermutation associated with APOBEC3G and 3F occurs at the 5′-G residue in a GG or GA viral DNA context (Bishop et al., 2006; Harris et al., 2003). In rare circumstances it was possible for G to A substitutions to be induced by Taq DNA polymerase, but errors involving Taq DNA polymerase selectively increase the rate of G to A substitution. These results suggest that hypermutation of TTV is induced by APOBEC3G and 3F.

We reported recently that interferon (IFN) increases the transcription of APOBEC3G and enhances the effects of the protein *in vitro* (Noguchi et al., 2007). Similar effects for IFN in enhancing the actions of APOBEC proteins have been reported in HIV studies (Bonvin et al., 2006; K. Chen et al., 2006; Peng et al., 2006; Tanaka et al., 2006). Thus, one can assume that the antiviral effect of APOBEC proteins should be enhanced by IFN and other cytokines *in vivo*. In this study, TTV DNA levels decreased during ALT flare-up in HBV carriers. It is assumed that ALT flare-up with exacerbation of chronic hepatitis is associated with increased production of various pro-inflammatory cytokines including IFN from infiltrating lymphocytes. Thus, we were expecting an increase in hypermutation of TTV genomes as well as HBV. However, while an increase in hypermutation of HBV was noted, no increase in hypermutation of TTV was observed because the serum TTV titers decreased to below the detection limits of 3D-PCR (Fig. 3). This finding is consistent with previous reports that demonstrated the sensitivity of TTV to immunological activation of the host (Chayama et al., 1999; Maggi

(a)

Patient	HBeAg	HBeAb	ALT	HBV DNA [log copy/ml]	Hypermutated HBV [/10^5 genomes]	TTV DNA [log copy/ml]
N1	−	−	N.D.	−	−	5.11
N2	−	−	N.D.	−	−	5.04
N3	−	−	N.D.	−	−	4.97
N4	−	−	N.D.	−	−	4.85
B1	+	−	87	8.8	722	5.52
B2	+	−	106	8.2	2916	5.44
B3	+	−	161	9.8	935	5.39
B4	+	−	42	8.8	750	5.32

(b)

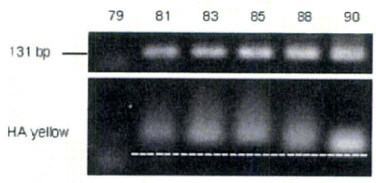

(c)

Td [°C]	79	81	83	85	88	90
N1	−	−	+	+	+	+
N2	−	−	+	+	+	+
N3	−	−	−	−	−	+
N4	−	−	−	−	−	+
B1	−	−	−	−	−	+
B2	−	−	−	−	+	+
B3	−	+	+	+	+	+
B4	−	−	−	−	+	+

Fig. 1. Detection of G to A hypermutation by 3D-PCR and electrophoresis. Hypermutated TTV genomes were detected in serum samples of four healthy individuals and four patients with HBV infection by 3D-PCR and visualized by gel electrophoresis. (a) Clinical data of selected healthy individuals and HBV carriers. (b) Analysis of 3D-PCR products by 2% agarose electrophoresis (upper panel) and HA yellow agarose gel electrophoresis (lower panel). Only a representative figure (B3 in panel [a]) is shown. (c) Presence of hypermutated TTV genomes in serum samples detected by 3D-PCR. N1–N4: healthy volunteers, B1–B4: patients with chronic hepatitis B, Td: denaturation temperature.

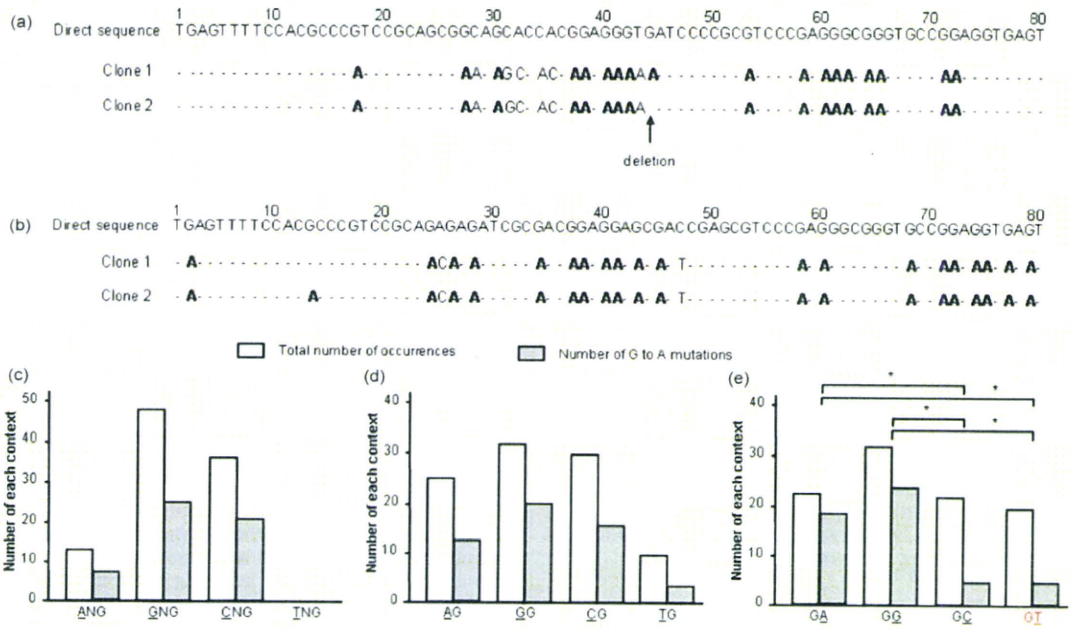

Fig. 2. Nucleotide sequences and context analysis of G to A hypermutated TTV genomes following 3D-PCR amplification, cloning and sequencing. (a and b) The 3D-PCR products were separated by electrophoresis on 2% (w/v) agarose gel, cloned and sequenced. The nucleotide sequences of two hypermutated clones obtained from B3 are shown. Only mutated residues are noted. (c–e) The preferred context of G to A hypermutation was analyzed using nucleotide sequences obtained by cloning and sequencing. The frequencies of nucleotides 2 (c) and 1 (d) nucleotides 5′ or 1 nucleotide 3′ (e) from the substituted G residues (underlined) were compared. The frequency of each context was analyzed with chi-square and Fisher's exact tests. *$P < 0.001$.

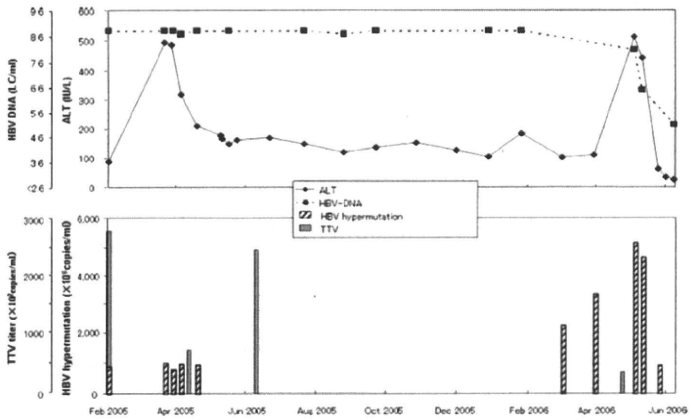

Fig. 3. Levels of hypermutated HBV genomes and TTV titers during HBV flare-ups. Serial changes in ALT, HBV DNA (top), TTV titer, and HBV hypermutation (bottom) in a patient with acute exacerbations of chronic hepatitis B. Note the increase in the levels of hypermutated HBV genomes during the exacerbations while the TTV titer was low and sometimes undetectable during such exacerbation by 3D-PCR.

et al., 2005) as well as to IFN treatment (Chayama et al., 1999). Altogether, the immune responses to HBV infection might activate the elimination of both HBV and TTV and might be the reason for the significant reductions of HBV and TTV serum titers, although the role of APOBEC3 proteins in this process is uncertain.

G to A hypermutation within viral genomes has been speculated to induce the production of dead viruses, the degradation of viral genomes by uracil DNA glycocylase and the impairment of viral replication. In the present study, we analyzed G to A hypermutation of TTV in the 5′-terminal non-coding region, which includes the TATA box and functions in transcriptional regulation. Thus we consider that G to A hypermutation in TTV may have a large impact on TTV replication. We propose that the association between TTV transcriptional activity and G to A hypermutation of TTV in human hepatocytes should be investigated further.

5. Conclusions

We showed in the present study the presence of hypermutated TTV genomes in sera of healthy individuals as well as HBV carriers. Further studies on other viruses with different replication mechanisms are necessary to clarify the interaction between APOBEC3 proteins and virus genomes. Analysis of viruses with established *in vitro* culture systems will be useful to study the mechanism of host antiviral innate immunity and the role of APOBEC3 proteins in the virus eradication process.

Acknowledgments

This work was supported in part by a Grant-in-Aid for Scientific Research and Development from the Ministry of Education, Sports, Culture, and Technology and the Ministry of Health, Labor and Welfare. This work was carried out at the Research Center for Molecular Medicine, Faculty of Medicine, Hiroshima University and the Analysis Center of Life Science, Hiroshima University. The authors thank Yoshiko Nakata and Aya Furukawa for secretarial assistance.

References

Ball, J.K., Curran, R., Berridge, S., Grabowska, A.M., Jameson, C.L., Thomson, B.J., Irving, W.L., Sharp, P.M., 1999. TT virus sequence heterogeneity in vivo: evidence for co-infection with multiple genetic types. J. Gen. Virol. 80 (Pt 7), 1759–1768.

Bishop, K.N., Holmes, R.K., Malim, M.H., 2006. Antiviral potency of APOBEC proteins does not correlate with cytidine deamination. J. Virol. 80 (17), 8450–8458.

Bishop, K.N., Holmes, R.K., Sheehy, A.M., Malim, M.H., 2004. APOBEC-mediated editing of viral RNA. Science 305 (5684), 645.

Bonvin, M., Achermann, F., Greeve, I., Stroka, D., Keogh, A., Inderbitzin, D., Candinas, D., Sommer, P., Wain-Hobson, S., Vartanian, J.P., Greeve, J., 2006. Interferon-inducible expression of APOBEC3 editing enzymes in human hepatocytes and inhibition of hepatitis B virus replication. Hepatology 43 (6), 1364–1374.

Chayama, K., Kobayashi, M., Tsubota, A., Kobayashi, M., Arase, Y., Suzuki, Y., Saitoh, S., Murashima, N., Ikeda, K., Okamoto, K., Hashimoto, M., Matsuda, M., Koike, H., Kobayashi, M., Kumada, H., 1999. Susceptibility of TT virus to interferon therapy. J. Gen. Virol. 80 (Pt 3), 631–634.

Chen, H., Lilley, C.E., Yu, Q., Lee, D.V., Chou, J., Narvaiza, I., Landau, N.R., Weitzman, M.D., 2006a. APOBEC3A is a potent inhibitor of adeno-associated virus and retrotransposons. Curr. Biol. 16 (5), 480–485.

Chen, K., Huang, J., Zhang, C., Huang, S., Nunnari, G., Wang, F.X., Tong, X., Gao, L., Nikisher, K., Zhang, H., 2006b. Alpha interferon potently enhances the anti-human immunodeficiency virus type 1 activity of APOBEC3G in resting primary CD4 T cells. J. Virol. 80 (15), 7645–7657.

Conticello, S.G., Langlois, M.A., Yang, Z., Neuberger, M.S., 2007. DNA deamination in immunity: AID in the context of its APOBEC relatives. Adv. Immunol. 94, 37–73.

Delebecque, F., Suspene, R., Calattini, S., Casartelli, N., Saib, A., Froment, A., Wain-Hobson, S., Gessain, A., Vartanian, J.P., Schwartz, O., 2006. Restriction of foamy viruses by APOBEC cytidine deaminases. J. Virol. 80 (2), 605–614.

Ganem, D., 2001. Virology. The X files—one step closer to closure. Science 294 (5550), 2299–2300.

Harris, R.S., Bishop, K.N., Sheehy, A.M., Craig, H.M., Petersen-Mahrt, S.K., Watt, I.N., Neuberger, M.S., Malim, M.H., 2003. DNA deamination mediates innate immunity to retroviral infection. Cell 113 (6), 803–809.

Hino, S., 2002. TTV, a new human virus with single stranded circular DNA genome. Rev. Med. Virol. 12 (3), 151–158.

Kao, J.H., Chen, W., Chen, P.J., Lai, M.Y., Chen, D.S., 2000. TT virus infection in patients with chronic hepatitis B or C: influence on clinical, histological and virological features. J. Med. Virol. 60 (4), 387–392.

Kijak, G.H., Janini, M., Tovanabutra, S., Sanders-Buell, E.E., Birx, D.L., Robb, M.L., Michael, N.L., McCutchan, F.E., 2007. HyperPack: a software package for the study of levels, contexts, and patterns of APOBEC-mediated hypermutation in HIV. AIDS Res. Hum. Retroviruses 23 (4), 554–557.

Lecossier, D., Bouchonnet, F., Clavel, F., Hance, A.J., 2003. Hypermutation of HIV-1 DNA in the absence of the Vif protein. Science 300 (5622), 1112.

Lochelt, M., Romen, F., Bastone, P., Muckenfuss, H., Kirchner, N., Kim, Y.B., Truyen, U., Rosler, U., Battenberg, M., Saib, A., Flory, E., Cichutek, K., Munk, C., 2005. The antiretroviral activity of APOBEC3 is inhibited by the foamy virus accessory Bet protein. Proc. Natl. Acad. Sci. U.S.A. 102 (22), 7982–7987.

Maggi, F., Tempestini, E., Lanini, L., Andreoli, E., Fornai, C., Giannecchini, S., Vatteroni, M., Pistello, M., Marchi, S., Ciccorossi, P., Specter, S., Bendinelli, M., 2005. Blood levels of TT virus following immune stimulation with influenza or hepatitis B vaccine. J. Med. Virol. 75 (2), 358–365.

Mangeat, B., Turelli, P., Caron, G., Friedli, M., Perrin, L., Trono, D., 2003. Broad antiretroviral defence by human APOBEC3G through lethal editing of nascent reverse transcripts. Nature 424 (6944), 99–103.

Mariani, R., Chen, D., Schrofelbauer, B., Navarro, F., Konig, R., Bollman, B., Munk, C., Nymark-McMahon, H., Landau, N.R., 2003. Species-specific exclusion of APOBEC3G from HIV-1 virions by Vif. Cell 114 (1), 21–31.

Nishizawa, T., Okamoto, H., Konishi, K., Yoshizawa, H., Miyakawa, Y., Mayumi, M., 1997. A novel DNA virus (TTV) associated with elevated transaminase levels in posttransfusion hepatitis of unknown etiology. Biochem. Biophys. Res. Commun. 241 (1), 92–97.

Noguchi, C., Hiraga, N., Mori, N., Tsuge, M., Imamura, M., Takahashi, S., Fujimoto, Y., Ochi, H., Abe, H., Maekawa, T., Yatsuji, H., Shirakawa, K., Takaori-Kondo, A., Chayama, K., 2007. Dual effect of APOBEC3G on hepatitis B virus. J. Gen. Virol. 88 (Pt 2), 432–440.

Noguchi, C., Imamura, M., Tsuge, M., Hiraga, N., Mori, N., Miki, D., Kimura, T., Takahashi, S., Fujimoto, Y., Ochi, H., Abe, H., Maekawa, T., Tateno, C., Yoshizato, K., Chayama, K., 2009. G-to-A hypermutation in hepatitis B virus (HBV) and clinical course of patients with chronic HBV infection. J. Infect. Dis. 199 (11), 1599–1607.

Noguchi, C., Ishino, H., Tsuge, M., Fujimoto, Y., Imamura, M., Takahashi, S., Chayama, K., 2005. G to A hypermutation of hepatitis B virus. Hepatology 41 (3), 626–633.

Norder, H., Courouce, A.M., Magnius, L.O., 1994. Complete genomes, phylogenetic relatedness, and structural proteins of six strains of the hepatitis B virus, four of which represent two new genotypes. Virology 198 (2), 489–503.

Peng, G., Lei, K.J., Jin, W., Greenwell-Wild, T., Wahl, S.M., 2006. Induction of APOBEC3 family proteins, a defensive maneuver underlying interferon-induced anti-HIV-1 activity. J. Exp. Med. 203 (1), 41–46.

Rosler, C., Kock, J., Kann, M., Malim, M.H., Blum, H.E., Baumert, T.F., von Weizsacker, F., 2005. APOBEC-mediated interference with hepadnavirus production. Hepatology 42 (2), 301–309.

Russell, R.A., Wiegand, H.L., Moore, M.D., Schafer, A., McClure, M.O., Cullen, B.R., 2005. Foamy virus Bet proteins function as novel inhibitors of the APOBEC3 family of innate antiretroviral defense factors. J. Virol. 79 (14), 8724–8731.

Suspene, R., Guetard, D., Henry, M., Sommer, P., Wain-Hobson, S., Vartanian, J.P., 2005a. Extensive editing of both hepatitis B virus DNA strands by APOBEC3 cytidine deaminases in vitro and in vivo. Proc. Natl. Acad. Sci. U.S.A. 102 (23), 8321–8326.

Suspene, R., Henry, M., Guillot, S., Wain-Hobson, S., Vartanian, J.P., 2005b. Recovery of APOBEC3-edited human immunodeficiency virus G → A hypermutants by differential DNA denaturation PCR. J. Gen. Virol. 86 (Pt 1), 125–129.

Suspene, R., Sommer, P., Henry, M., Ferris, S., Guetard, D., Pochet, S., Chester, A., Navaratnam, N., Wain-Hobson, S., Vartanian, J.P., 2004. APOBEC3G is a single-stranded DNA cytidine deaminase and functions independently of HIV reverse transcriptase. Nucleic Acids Res. 32 (8), 2421–2429.

Tanaka, Y., Marusawa, H., Seno, H., Matsumoto, Y., Ueda, Y., Kodama, Y., Endo, Y., Yamauchi, J., Matsumoto, T., Takaori-Kondo, A., Ikai, I., Chiba, T., 2006. Anti-viral protein APOBEC3G is induced by interferon-alpha stimulation in human hepatocytes. Biochem. Biophys. Res. Commun. 341 (2), 314–319.

Zhang, H., Yang, B., Pomerantz, R.J., Zhang, C., Arunachalam, S.C., Gao, L., 2003. The cytidine deaminase CEM15 induces hypermutation in newly synthesized HIV-1 DNA. Nature 424 (6944), 94–98.

Published April 18, 2011

THE JOURNAL OF CELL BIOLOGY

miR-22 represses cancer progression by inducing cellular senescence

Dan Xu,[1] Fumitaka Takeshita,[3] Yumiko Hino,[1] Saori Fukunaga,[1] Yasusei Kudo,[2] Aya Tamaki,[1] Junko Matsunaga,[1] Ryou-u Takahashi,[3] Takashi Takata,[2] Akira Shimamoto,[1] Takahiro Ochiya,[3] and Hidetoshi Tahara[1]

[1]Department of Cellular and Molecular Biology and [2]Department of Oral Maxillofacial Pathobiology, Graduate School of Biomedical Science, Hiroshima University, Minami-ku, Hiroshima 734-8553, Japan
[3]Division of Molecular and Cellular Medicine, National Cancer Center Research Institute, Chuo-ku, Tokyo 104-0045, Japan

Cellular senescence acts as a barrier to cancer progression, and microRNAs (miRNAs) are thought to be potential senescence regulators. However, whether senescence-associated miRNAs (SA-miRNAs) contribute to tumor suppression remains unknown. Here, we report that miR-22, a novel SA-miRNA, has an impact on tumorigenesis. miR-22 is up-regulated in human senescent fibroblasts and epithelial cells but down-regulated in various cancer cell lines. miR-22 overexpression induces growth suppression and acquisition of a senescent phenotype in human normal and cancer cells. miR-22 knockdown in presenescent fibroblasts decreased cell size, and cells became more compact. miR-22–induced senescence also decreases cell motility and inhibits cell invasion in vitro. Synthetic miR-22 delivery suppresses tumor growth and metastasis in vivo by inducing cellular senescence in a mouse model of breast carcinoma. We confirmed that CDK6, SIRT1, and Sp1, genes involved in the senescence program, are direct targets of miR-22. Our study provides the first evidence that miR-22 restores the cellular senescence program in cancer cells and acts as a tumor suppressor.

Introduction

Tumor progression is a multistep process wherein several defined events are common to cancer cells, such as uncontrolled proliferation and invasion (Hahn and Weinberg, 2002). Cellular senescence is characterized by an irreversible arrest of cell proliferation, so that it can prevent the aberrant and unlimited proliferation of tumor cells (Campisi, 2005). Senescent cells exhibit enlarged morphological changes and less motility than young cells, which may contribute to the suppression of cell migration, invasion, and metastasis (Chen et al., 2000). Oncogene-induced senescence is a cellular response, which can occur in vivo and provides a bona fide barrier to tumorigenesis (Narita and Lowe, 2005). Oncogene-induced senescence was found in premalignant tumors but not in more advanced malignant tumors (Braig et al., 2005; Collado et al., 2005). Therefore, cellular senescence acts as an important barrier to cancer and plays an important role in tumor suppression.

Correspondence to Hidetoshi Tahara: toshi@hiroshima-u.ac.jp

Abbreviations used in this paper: cont miR, control miRNA; HPA, hybridization protection assay; hTERT, human telomerase reverse transcriptase; LNA, locked nucleic acid; miRNA, microRNA; PDL, population doubling level; pRb, retinoblastoma protein; SA-β-gal, senescence-associated β-galactosidase; SAHF, senescence-associated heterochromatin foci; SA-miRNA, senescence-associated miRNA; UTR, untranslated region; WT, wild type.

The Rockefeller University Press $30.00
J. Cell Biol. Vol. 193 No. 2 409–424
www.jcb.org/cgi/doi/10.1083/jcb.201010100

microRNAs (miRNAs) are a class of naturally occurring small noncoding RNAs that negatively regulate the stability and translation of target protein–coding mRNAs at the 3′ untranslated region (UTR). miRNAs typically target a cluster of genes rather than one specific gene (Bartel, 2004), a characteristic which allows them to play critical roles in a variety of biological processes such as cell proliferation, differentiation, apoptosis, and carcinogenesis (He and Hannon, 2004). Recently, a growing number of studies have documented the miRNA expression profiles in human cancers (Calin and Croce, 2006), suggesting that miRNAs emerge as novel biomarkers for various cancers. However, there is currently little information about miRNA profiling studies and biological effects of miRNAs in cellular senescence.

The senescence program is established and maintained by p53 and retinoblastoma protein (pRb) tumor suppressor pathways. The requirements of p53 and pRb for the induction of cellular senescence vary in their prominence depending on the genetic context, species, and cell type (Adams, 2007; Schmitt, 2007;

Supplemental Material can be found at:
http://jcb.rupress.org/content/suppl/2011/04/18/jcb.201010100.DC1.html
Original image data can be found at:
http://jcb-dataviewer.rupress.org/jcb/browse/4262

Published April 18, 2011

Haferkamp et al., 2009). Recently, various studies have indicated that some miRNAs, such as miR-34a and miR-20a, induce senescence-like growth arrest through regulating cell cycle genes and senescence-associated genes involved in the p53 and/or pRb pathway (Tazawa et al., 2007; Poliseno et al., 2008; Sun et al., 2008). Such miRNAs play a direct role in senescence and are called senescence-associated miRNAs (SA-miRNAs; Lafferty-Whyte et al., 2009).

In the present study, we attempted to screen SA-miRNAs that control cellular senescence in human fibroblasts, and we report here that miR-22 is a novel SA-miRNA that functions in mediating cellular senescence. We studied the role of miR-22 in cellular senescence using human normal cells and cancer cell lines as an in vitro culture system as well as an in vivo mouse breast tumor model. Upon senescence, cells become flattened and enlarged and exhibit biochemical changes such as the increased perinuclear activity of senescence-associated β-galactosidase (SA-β-gal; Dimri et al., 1995; Narita et al., 2003). Another critical event during the cellular senescence process is a decrease in cell growth and cell motility. We found a widespread decrease of miR-22 expression in various human cancer cell lines. Introduction of miR-22 into cancer cells inhibits cell proliferation, accompanied by senescence-like cell morphology and a decrease in cell motility and invasiveness. We predicted the putative direct targets of miR-22 by the computational prediction of targets based on sequence match to the miRNA. We identified three targets, including CDK6, Sp1, and SIRT1, which are directly regulated by miR-22. Furthermore, silencing of these targets resulted in growth arrest and increased SA-β-gal activity, accompanied by pRB dephosphorylation. We confirmed that miR-22 regulated the pRb pathway of cellular senescence through targeting of CDK6 and SIRT1. Ectopic expression of CDK6, SIRT1, or Sp1 could partially rescue the senescence phenotypes in miR-22–transfected cells. Significantly, miR-22 injection suppresses tumor growth and metastasis in vivo by induction of senescence in breast tumor, suggesting that SA-miRNA miR-22 acts as an important barrier to cancer and plays an important role in tumor suppression. Our findings provide new insight for the role of SA-miRNAs between cellular senescence and tumorigenesis.

Results

miR-22 overexpression induces cellular senescence in human fibroblasts

To identify miRNAs that control cellular senescence, we analyzed miRNA expression profiling by miRCURY locked nucleic acid (LNA) miRNA array in young and senescent TIG-3 fibroblasts (Fig. 1 A). We found that a set of altered expression miRNAs has been reported to be involved in cell growth and tumorigenesis (Fig. 1 A and Table S1). Among them, the majority of antigrowth miRNAs were expressed two– to fourfold more in senescent TIG-3 cells than in young cells. To confirm and validate the results, we performed 3D-Gene miRNA microarray to evaluate miRNA expression levels. Two kinds of microarray analysis showed that five miRNAs are uniformly up-regulated by twofold or greater in senescent compared with young cells. These include miR-22, miR-34a, miR-125a-5p, miR-24-2*, and miR-152, several of which, namely miR-34a and miR-125a-5p, are closely associated with senescence-like growth arrest and metastasis in cancer cells (Tazawa et al., 2007; Li et al., 2009; Wang et al., 2009). Here, we focused on miR-22 and evaluated the expression of miR-22 in young and senescent human diploid fibroblast strains. Quantitative (q) RT-PCR analysis confirmed that miR-22 expression was increased in senescent TIG-3 and other fibroblasts and even up-regulated by more than fivefold in senescent MRC-5 cells (Fig. 1 B). These findings suggest that miR-22 up-regulation is universal in senescent human fibroblasts.

To investigate the involvement of miR-22 in cellular senescence in human fibroblasts, we enforced miR-22 expression by introduction of mature miR-22 duplex into young fibroblasts. We first examined miR-22 expression level by qRT-PCR analysis at day 6 after direct transfection with miR-22 duplex into young MRC-5 cells (Fig. 1 C). Compared with the endogenous level of miR-22 in the senescent MRC-5 cells (fivefold higher than young cells), miR-22 was up-regulated by 2.9-fold (1 nM), 4-fold (5 nM), and 15.7-fold (10 nM) in MRC-5 cells, relative to control miRNA (cont miR) in each transfection group. Furthermore, miR-22 also increased SA-β-gal activity (Fig. 1 D), a well known senescence cytosolic biomarker, in a transfection dose-dependent manner, whereas cont miR did not induce SA-β-gal activity. These results imply that up-regulation of miR-22 expression is significant for the induction of senescence phenotypes. Because the cessation of cell proliferation is a hallmark of cellular senescence, we examined whether cell proliferation is altered by overexpression of miR-22. We observed that transfection of 10 nM miR-22 caused a remarkable inhibition of cell proliferation compared with that of cont miR (Fig. 1 E), and this growth inhibition by miR-22 is in a dose-dependent manner (not depicted). Senescence-associated heterochromatin foci (SAHF) formation is thought to be a senescence nuclei biomarker and is often observed in senescent fibroblasts (Dimri et al., 1995; Narita et al., 2003; Adams, 2007). We observed obvious SAHF formation in miR-22–transfected cells, and the percentage of SAHF-positive cells was significantly increased by miR-22 overexpression and was also increased in senescent MRC-5 cells (Fig. 1 F). This result is not cell type specific because other fibroblasts, such as IMR90, transfected with miR-22 appeared to be senescence phenotypes (unpublished data).

To ensure that the function of mature miRNA is not at a supraphysiological level, we repeated these experiments using a stable miRNA vector that mimics miRNA biological processing. Pre–miR-22 lentiviral construct (Lenti-Pre22), stably expressing miR-22 precursor in its native context, was used to study the effect of miR-22 on cellular senescence in MRC-5 fibroblasts. Lenti-Pre22–infected cells exhibited the enlarged senescence morphology and SA-β-gal–positive staining (Fig. 2 A). Compared with Lentiviral empty vector (Lenti-C), Lenti-Pre22 infection significantly increased SA-β-gal activity and caused growth arrest in MRC-5 cells (Fig. 2, A and B), which is similar to the effect of mature miR-22. Collectively, these results suggest that miR-22 is associated with cellular senescence, accompanied by the induction of major specific senescence-associated markers in human diploid fibroblasts.

Published April 18, 2011

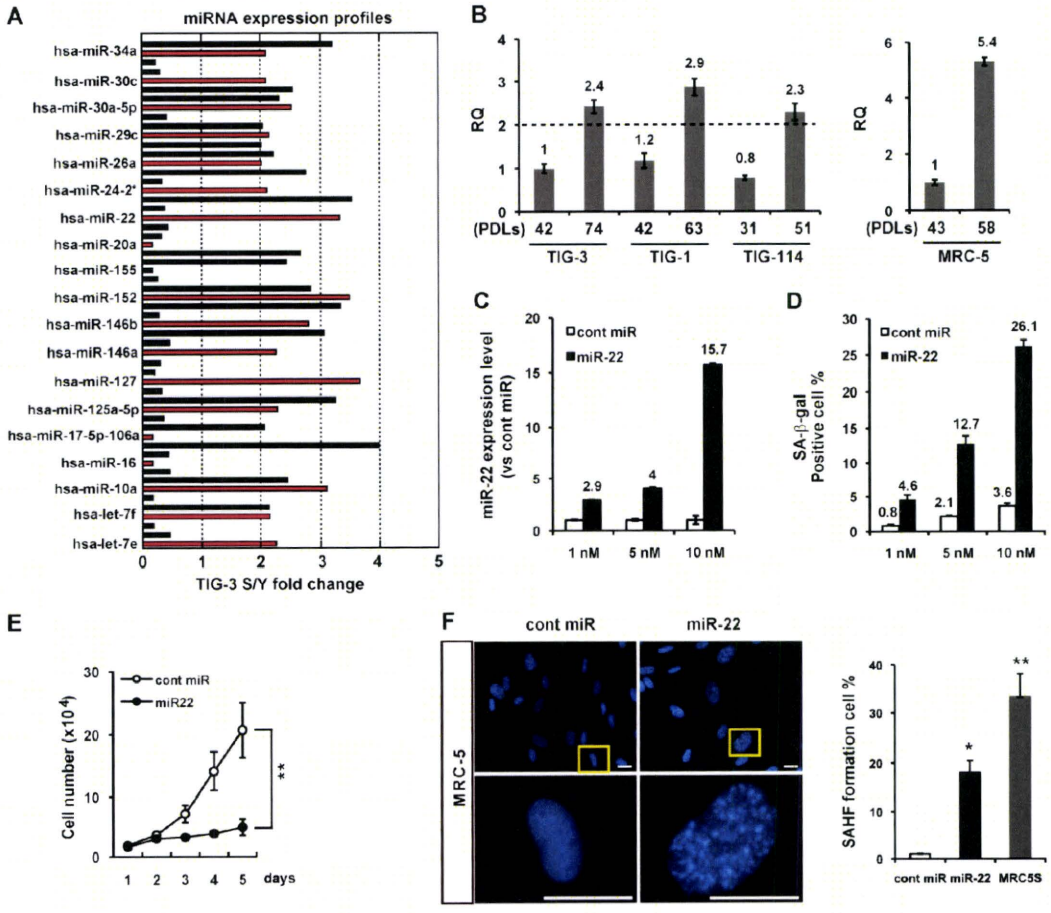

Figure 1. **miR-22 is up-regulated in senescent human fibroblasts, mediating cellular senescence.** (A) miRNA expression profile of TIG-3 fibroblasts was analyzed by miRNA microarray, presented as fold changes in miRNA expression between TIG-3S (senescent) and young (Y) cells. A set of altered expression miRNAs is indicated by red columns (see Table S1). RQ, relative quantitation. (B) Relative quantitation of miR-22 expression in different PDLs of fibroblasts was analyzed by qRT-PCR analysis. miR-22 expression levels in human fibroblasts were indicated, relative to those in TIG-3 (42 PDL) set at 1 in the left histogram and MRC-5 (43 PDL) set at 1 in the right histogram. U6 was used as an internal normalization control. The dashed line represents the threshold of expression level (twofold vs. TIG-3 42 PDL). (C and D) MRC-5 cells were transfected with cont miR or mature miR-22 (miR-22) for 6 d at indicated concentration. (C) qRT-PCR analysis shows the relative quantitation of miR-22 expression (vs. cont miR) in each transfection group. miR-22 expression levels in miR-22–transfected MRC-5 cells were indicated, relative to that in cont miR–transfected cells set at 1. U6 was used as an internal normalization control. (D) SA-β-gal activity was presented by the percentage of SA-β-gal–positive cells, which was indicated in different dose groups. (E) Cell proliferation assay was performed after transfection of 10 nM miR-22 or cont miR, and cells were counted for the indicated days. Each value was determined in triplicate. **, $P < 0.01$. (F) Representative photos for SAHF formation in MRC-5 cells at day 6 after transfection. Images were taken with fluorescence microscopy. Enlarged images of the boxed area from the top are shown in the bottom. SAHF formation was quantified by counting 200 cells from >10 random fields, and the results were shown in the right histogram in contrast to MRC5S (senescent; 58 PDL). Data in all the panels represent mean ± SEM ($n = 3$). *, $P < 0.05$; **, $P < 0.01$. Bars, 20 μm.

Furthermore, we wondered how knockdown of miR-22 impacts cellular senescence phenotypes and whether a reduced expression of miR-22 would impede the progression of senescence and extend the life span in fibroblasts. miRZip anti–miR-22 expression lentivector (anti-22), which can stably express anti–miR-22 and provide permanent miR-22 inhibition, was used to infect young (44 population doubling level [PDL]) and presenescent (54 PDL) MRC-5 cells. We observed that Leni-Pre22–infected young MRC-5 cells demonstrated enlarged senescent morphological changes (Fig. 2 C, GFP-labeled cells marked with yellow arrowheads). In contrast, anti-22–infected young MRC-5 cells seemed smaller and younger than anti-22 empty vector (anti-C)–treated cells (Fig. 2 D). For presenescent MRC-5 cells, stable knockdown of miR-22 caused obvious morphological changes, exhibiting small and thin morphology (Fig. 2 C, GFP-labeled cells marked with arrows), whereas those cells that failed to be infected exhibited enlarged senescent morphology (Fig. 2 C, white triangles) within the same field under the fluorescent microscope. Presenescent MRC-5 cells entered senescence and demonstrated obvious SA-β-gal staining as time passed. Anti-22–infected presenescent MRC-5 cells maintained small and thin morphology for >2 wk with a decreased percentage of SA-β-gal–positive cells (Fig. 2 E), and there appeared to be a significant decrease in cell size and percentage of cells

Published April 18, 2011

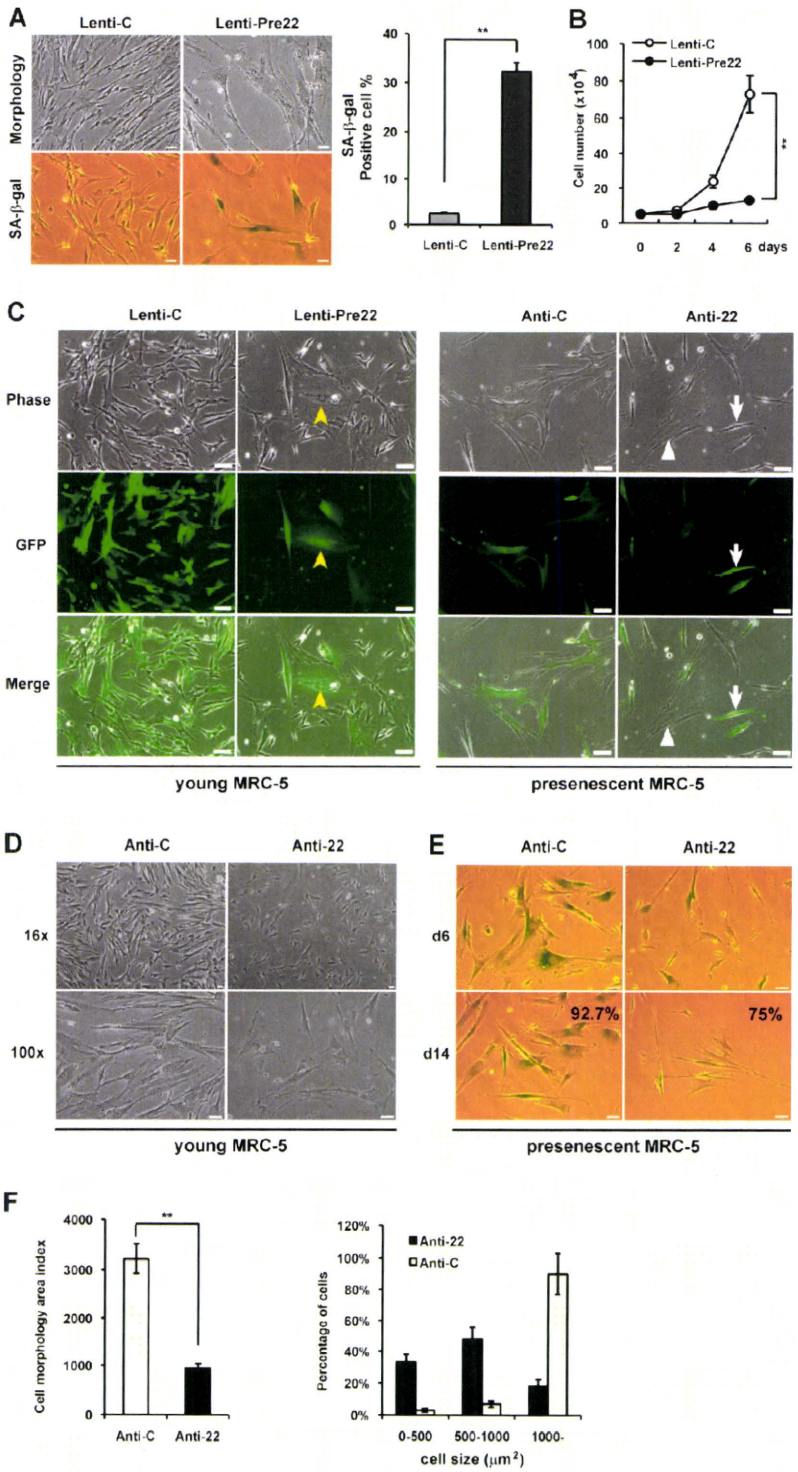

Figure 2. **Stable expression and knockdown of miR-22 affect senescence phenotypes in MRC-5 cells.** (A) Cell morphology and SA-β-gal activity were analyzed by phase-contrast microscopy at day 6 after infection with empty vector (Lenti-C) or premiR-22 (Lenti-Pre22). The percentage of SA-β-gal–positive cells is presented in the right histogram. (B) Cell proliferation assay was performed after infection of Lenti-Pre22, and cells were counted for the indicated days, compared with control cells. Each value was determined in triplicate. **, $P < 0.01$. (C) Cell morphology was analyzed with fluorescence microscopy at day 6 after infection. GFP-labeled cells indicate infected cells (middle). Yellow arrowheads and white arrows depict miR-22 overexpression in young MRC-5 cells and miR-22 knockdown in presenescent MRC-5 cells, respectively. Those cells that failed to be infected are marked with white triangles. (D) Cell morphology of anti-22–infected young MRC-5 was analyzed by phase-contrast microscopy and compared with anti-C. (E) Presenescent MRC-5 cells infected with anti-C or anti-22 were subjected to SA-β-gal assay at days 6 and 14 after infection. The percentage of SA-β-gal–positive cells at day 14 after infection is presented in the bottom panels. (F) Cell morphology area and cell size distribution were analyzed using ImageJ by counting GFP-expressed presenescent MRC-5 cells after infection with anti-C or anti-22 for 6 d. Cell morphology area index represents cell size (micrometers squared). Cell size distribution was divided into three groups: 0–500, 500–1,000, and 1,000 μm^2 and up. Data in all the panels represent mean ± SEM ($n = 3$). **, $P < 0.01$. Bars: (A, D, and E) 50 μm; (C) 20 μm.

distributed in a large-sized group (Fig. 2 F), compared with senescent anti-C–treated cells. Although stable knockdown of miR-22 exhibited neither the promotion of cell proliferation nor the extension of the life span (not depicted), this might be a result of irreversible growth arrest in senescent cells. These findings suggest the requirement of miR-22 in mediating senescence and indicate that miR-22 inhibition is indeed an obstacle for the progression of senescence in fibroblasts.

Published April 18, 2011

miR-22 overexpression induces growth suppression and senescence-like phenotypes in human breast epithelial and cancer cells

Senescence has been most widely studied in fibroblasts in vitro but is also well defined in other cell types, such as epithelial cells which are the origin of most carcinoma (Narita et al., 2003). Expression of human telomerase reverse transcriptase (hTERT) in certain cell types has been shown to extend cellular life span without malignant transformation. To investigate the effect of miR-22 on cellular senescence in human epithelial cells, we used hTERT-infected HMEC184 (184hTERT) cells that possess the unlimited proliferation capacity of HMEC184 cells and are regarded as immortalized. We found that miR-22 was expressed higher by >2.5-fold in senescent HMEC184 (22 PDL) than in 184hTERT cells that have a similar miR-22 expression level to that of normal young HMEC184 (Fig. 3 A). Compared with immortalized 184hTERT cells, a widespread decrease in miR-22 level was observed in various human cancer cells (Fig. 3 A), indicating that miR-22 may have an intrinsic function in tumor suppression associated with various human malignancies.

To test this notion, we first evaluated the effect of miR-22 on cell growth and SA-β-gal activity in human breast epithelial cells and two breast cancer cell lines. We found that miR-22 significantly inhibited cell growth in 184hTERT, MCF7, and MDA-MB-231-luc-D3H2LN (called MDA-D3 for short; Fig. 3 B). We noted that mature miR-22 caused remarkable and characteristic morphological alterations, including enlarged cellular size and a flattened shape (Fig. 3 C), and significantly increased SA-β-gal activity in the three cells (Fig. 3 D). Furthermore, we confirmed that overexpression of premiR-22 in MDA-D3 cells also significantly induced senescence-specific morphological changes, increased SA-β-gal activity (Fig. 3 E), and inhibited cell growth (Fig. 3 F), similar to the effect of mature miR-22.

The marked induction of senescence by miR-22 in human breast cancer cells prompted us to investigate whether miR-22 induces cellular senescence in other human cancer cells. Therefore, we further studied the effect of miR-22 in the human cervical carcinoma cell line SiHa. We confirmed the dose-dependent increase in miR-22 expression level (Fig. 4 A) and SA-β-gal activity (Fig. 4 B) after direct transfection of miR-22 in SiHa cells, whereas cont miR affected neither the cell growth nor the SA-β-gal activity. Introduction of 10 nM miR-22 resulted in cells exhibiting a senescence-like flattened shape and SA-β-gal–positive staining (Fig. 4 C), and it induced remarkable growth suppression compared with that of cont miR (Fig. 4 D). Because senescent cells never reenter the cell cycle and appear to decrease in DNA synthesis, we performed FACS analysis and quantity analysis of BrdU incorporation in SiHa cells. miR-22 overexpression induced cell cycle arrest at G1 phase, accompanied by the decrease in percentages of S phase (Fig. 4 E). The inhibitory effect of miR-22 on cell cycle progression has also been recently reported in other cancer cells (Ting et al., 2010). Furthermore, miR-22 resulted in the decrease of BrdU incorporation in comparison with cont miR or miR-34a (Fig. 4 F), indicating impaired DNA replication in miR-22–transfected cells during the S phase of the cell cycle. In addition, we confirmed that miR-22 expression was increased in Lenti-Pre22–infected SiHa cells (Fig. 4 G) close to the expression level of miR-22 (10 nM). Lenti-Pre22 also induced senescence-specific morphological changes, increased SA-β-gal activity, and inhibited cell growth (Fig. 4, H and I), indicating the induction of cellular senescence by miR-22 overexpression in SiHa cells.

Moreover, we did not observe any significant increase in TUNEL-positive apoptotic cells in miR-22–transfected SiHa and MDA-D3 cells (Fig. S1, A and B). These findings suggest that the growth suppression induced by miR-22 overexpression was caused by the induction of G1 arrest in cellular senescence rather than apoptosis. In reverse, miR-22 knockdown in cancer cells resulted in various morphological changes and differential timing of apoptosis in different cell lines. Anti-22–infected SiHa cells appeared to be small and underwent apoptosis at day 6 after infection (Fig. S1 C), whereas MDA-D3 cells became rounded and apoptotic cells were observed in anti-22–infected cells from the third day after infection (Fig. S1 D), which might be because the timelines for the progression of different cells through apoptosis vary in different cell lines (Jessel et al., 2002).

Various findings have suggested the critical role of telomere shortening in contributing to cellular senescence in human cells (Deng et al., 2008). Telomeric 3′-overhang (G-tail) is essential for proper telomere function (Tahara et al., 2005). Here, overexpression of miR-22 had no effect on the length of either total telomere or G-tail (Fig. S2), indicating that miR-22–induced senescence is possibly independent of telomere shortening.

SIRT1, Sp1, and CDK6 are direct targets of miR-22

miRNAs are known to suppress hundreds of mRNA targets, resulting in global changes in the cellular phenotype of cells (He and Hannon, 2004). We therefore make an effort to identify potential targets for miR-22 using both in silico and experimental approaches. We used a consensus approach with three widely used types of software (miRanda, TargetScan, and PicTar) to perform the target prediction. After overlapping prediction analysis, we screened those genes that were down-regulated upon senescence and implicated in cell growth and cell cycle regulation. Based on this, SIRT1, Sp1, and CDK6 were selected to be putative miR-22 target genes. The mRNAs of SIRT1 and Sp1 contain putative binding sites for miR-22 in their 3′-UTRs, and each site is broadly conservative among mammals. CDK6 mRNA contains three miR-22 binding sites in the 3′-UTR, whereas it is different in conservation for each site (Fig. 5 A).

To address those genes directly regulated by miR-22, we performed luciferase reporter assay. We constructed pmirGLO full-length 3′-UTR of both SIRT1 and Sp1. Because the full-length 3′-UTR of CDK6 is too long (~10 kbp), human CDK6 3′-UTR containing three binding sites (6 kbp) was amplified and cloned into pmirGLO vector. Furthermore, to study which site in the 3′-UTR of each gene is important, we engineered luciferase reporters that have exact binding sites of 3′-UTRs of these genes including the wild type (WT) and two mutant UTRs (Mut1 and Mut2), as shown in Fig. 5 C. In SiHa and MDA-D3 cells, miR-22 significantly reduced the luciferase activities of the full-length 3′-UTR (Fig. 5 B) or WT SIRT1, SP1, and CDK6

Published April 18, 2011

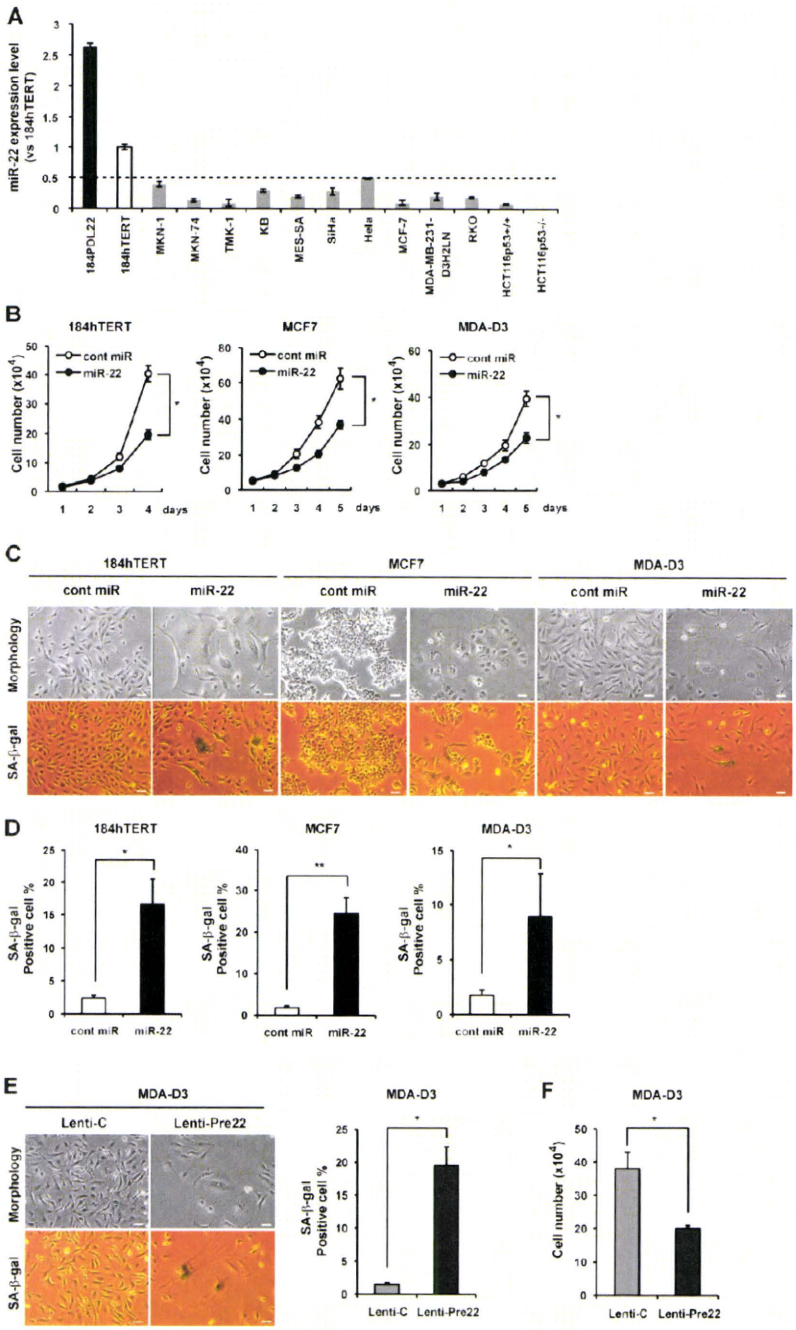

Figure 3. **Overexpression of miR-22 induces senescence-like phenotypes in human breast epithelial and breast cancer cells.** (A) qRT-PCR analysis shows relative quantitation of miR-22 expression level (vs. 184hTERT) in human epithelial and various cancer cells. Expression levels of miR-22 in various cells were relative to that in 184hTERT cells set at 1. U6 was used as an internal normalization control. The dashed line represents the threshold of expression level (0.5-fold vs. 184hTERT). (B) Cell proliferation assay was performed after transfection of miR-22, and cells were counted for the indicated days, compared with control cells. Each value was determined in triplicate. *, $P < 0.05$. (C–E) Cell morphology and SA-β-gal activity were analyzed by phase-contrast microscopy at day 6 after transfection (C and D) or infection (E) in indicated cells. SA-β-gal activity was presented by the percentage of SA-β-gal–positive cells. (F) Cell proliferation assay was performed at day 6 after MDA-D3 cells were infected with Lenti-Pre22 and compared with control cells. Data in all the panels represent mean ± SEM ($n = 3$). *, $P < 0.05$; **, $P < 0.01$. Bars, 50 μm.

(site 1 and site 3) reporters (Fig. 5 D), compared with the negative cont miR. In contrast, neither Mut1 (deletion of seed region) nor Mut2 of mutant reporters was repressed by miR-22, which indicates that these target sites directly mediate the repression (Fig. 5 E). In addition, this down-regulation was not seen in WT construct of CDK6 site 2, possibly because of poorly conserved sites among mammals. These results provide experimental evidence that miR-22 can directly repress translation initiation of SIRT1, SP1, and CDK6.

Western blot analysis showed that overexpression of miR-22 markedly down-regulated SIRT1, SP1, and CDK6 in SiHa and MDA-D3 cells (Fig. 5 F). Moreover, we confirmed that SIRT1 and CDK6 were down-regulated in senescent MRC-5 fibroblasts and HMEC184 epithelial cells, accompanied by a decrease in pRB phosphorylation at ser807/811 (Fig. 5 G). This indicates that SIRT1 and CDK6 are senescence-associated genes that are involved in cellular senescence possibly through the pRb pathway. Sp1 was not detected because of its low expression level in these cells.

Published April 18, 2011

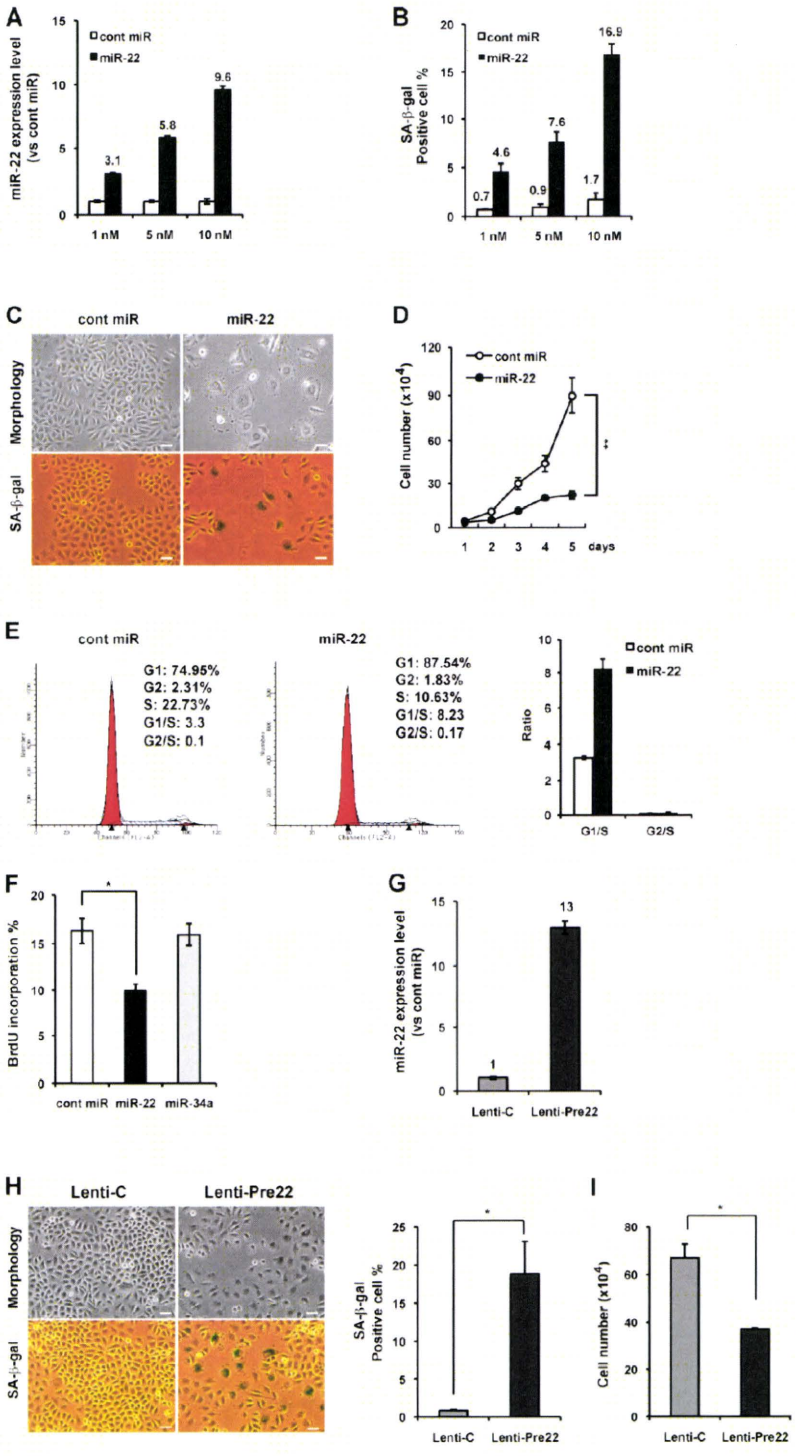

Figure 4. **Overexpression of miR-22 induced cellular senescence, cell cycle G1 arrest, and the decrease in BrdU incorporation in SiHa cells.** (A and B) SiHa cells were transfected with cont miR or miR-22 at the indicated concentration for 6 d. qRT-PCR results show the relative level of miR-22 expression to cont miR in each transfection group (A). SA-β-gal activity was presented by the percentage of SA-β-gal–positive cells (B). (C) Cell morphology and SA-β-gal activity were analyzed by phase-contrast microscopy at day 6 after transfection of 10 nM miR-22 or cont miR. (D) Cell proliferation assay was performed after transfection of 10 nM miR-22, and cells were counted for the indicated days, compared with control cells. Each value was determined in triplicate. **, $P < 0.01$. (E) Cell cycle analysis was performed at 48 h after transfection. The percentage of G1, S, and G2 are demonstrated as shown. The histogram displays the relative changes of G1 and G2 phase compared with S phase. (F) BrdU quantitative analysis was performed at 72 h after transfection, presented by the percentage of BrdU incorporation. (G) Stable expression of miR-22 (Lenti-Pre22) was evaluated by qRT-PCR analysis, presented by the relative quantitation of miR-22 expression level at day 6 after infection. Expression level of miR-22 in Lenti-Pre22–transfected cells was relative to that in Lenti-C–transfected cells set at 1. U6 was used as an internal normalization control. (H) Cell morphology and SA-β-gal activity were analyzed by phase-contrast microscopy at day 6 after infection. The percentage of SA-β-gal–positive cells is presented in the right histogram. (I) Cell proliferation assay was performed at day 6 after infection with Lenti-Pre22 and compared with control cells. Data in all the panels represent mean ± SEM ($n = 3$). *, $P < 0.05$; **, $P < 0.01$. Bars, 50 μm.

Furthermore, silencing of these target genes by siRNAs resulted in growth arrest (Fig. 6 A) and increased SA-β-gal activity in MRC-5 fibroblasts and MDA-D3 cells (Fig. 6 B), as well as morphological changes (not depicted), similar with miR-22–induced senescence phenotypes. We confirmed that the siRNAs against SIRT1 and CDK6 knocked down the expression of SIRT1 and CDK6 and caused dephosphorylation of pRB at ser807/811 (Fig. 6, C and E), which was also induced by either mature miR-22 or premiR-22 overexpression in various different cells (Fig. 6, D and F). In addition,

Published April 18, 2011

A

Gene	GenBank	Conservation	3'UTR Position on mRNA	Binding sites on 3'UTR	Target Site	Prediction algorism
SIRT1	NM_012238	H/P/M/R/D	2298-4089	514-536	3' UGUCAAGAAGUUG--ACCGUCGAA 5' (miR-22) 5' CAUUUUCCAAAACUGUGGCAGCUA 3' (UTR)	TargetScan, PicTar, miRanda
SP1	NM_138473	H/P/M/R/D	2456-7656	4719-4741	3' UGUCAAGAAGUUGACCGUCGAA 5' (miR-22) 5' CUACACACACCAGUGGCAGCUG 3' (UTR)	TargetScan, PicTar, miRanda
CDK6	NM_001259		1394-11628			
	Site-1	H/P/M/R/D		176-188	3' UGUCAAGAAGUUGACCGUCGAA 5' (miR-22) 5' AAUGCAAGAGUGAUUGCAGCUU 3' (UTR)	PicTar
	Site-2	H/P		1862-1884	3' UGUCAAGAAGUUGACCGUCGAA 5' (miR-22) 5' UGUACUGAAUUCUUUGCAGCUU 3' (UTR)	PicTar
	Site-3	H/P/D		5928-5950	3' UGUCAAGAAGUUGACCGUCGAA 5' (miR-22) 5' ACAGCACCACACAAAGCAGCUU 3' (UTR)	PicTar

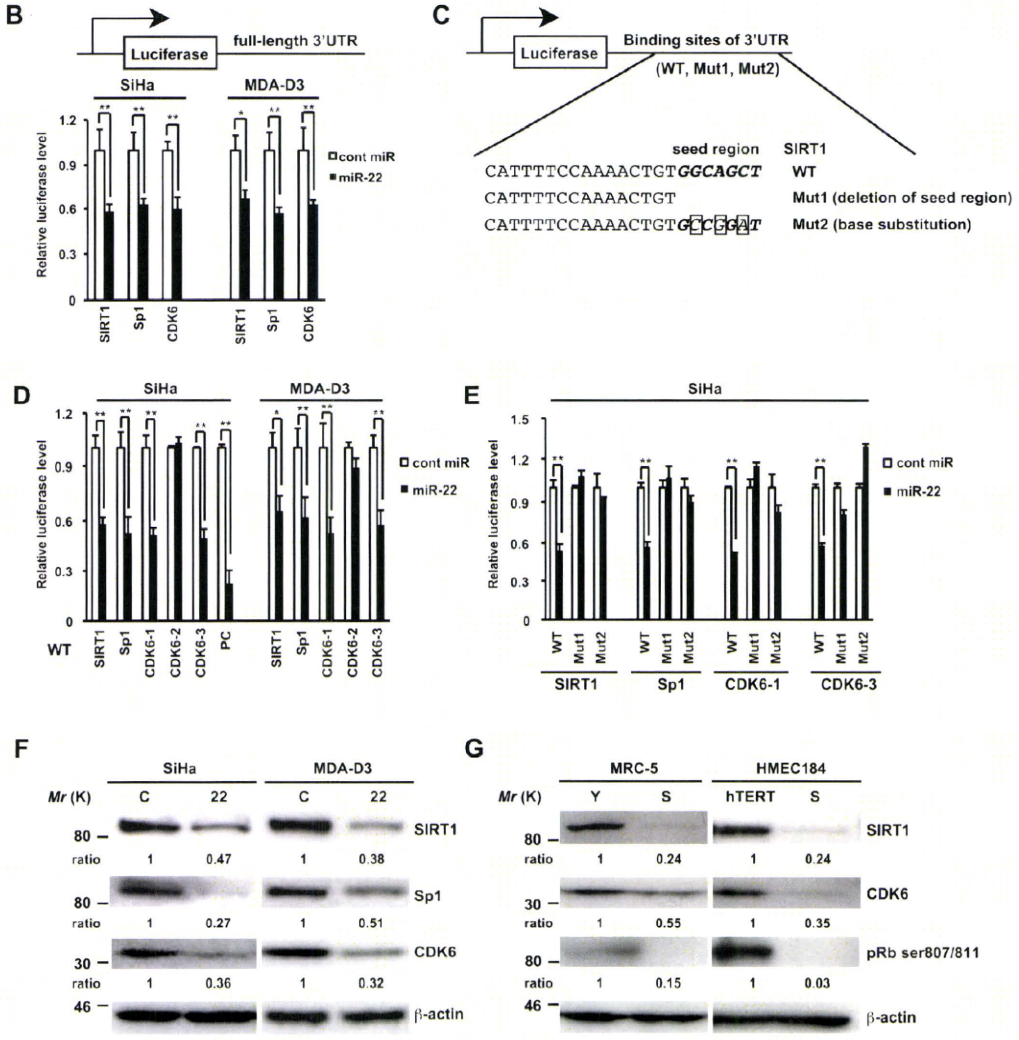

Figure 5. **SIRT1, Sp1, and CDK6 are direct targets of miR-22.** (A) Summary of miR-22 target sites in the 3′-UTR of SIRT1, Sp1, and CDK6. H, human; P, chimp; M, mouse; R, rat; D, dog. The underlined bold nucleotides indicate target sites. (B–E) Target validation of SIRT1, Sp1, and CDK6 was confirmed in the luciferase reporter assay. (C) Scheme of the luciferase reporter constructs containing conserved miR-22 target sites (WT), deletion of seed region (Mut1), or base substitution of seed region (Mut2) was indicated using SIRT1 as an example. The seed region is italic bold, and point mutations are boxed in the seed region. Each construct, including full-length 3′-UTR (B), WT (D), or Muts (E), was cotransfected with miR-22 or cont miR into SiHa or MDA-D3 cells. Relative luciferase level = $(S_{luc}/S_{renilla})/(C_{luc}/C_{renilla})$ in relative light units (RLUs). S_{luc}, RLUs of firefly luciferase activity in miR-22–transfected sample. $S_{renilla}$, RLUs of renilla luciferase activity in miR-22–transfected sample. C_{luc}, RLUs of firefly luciferase activity in cont miR–transfected groups. $C_{renilla}$, RLUs of renilla luciferase

Published April 18, 2011

p53 protein level did not change in MRC-5 and MDA-D3 cells, but p53 expression is up-regulated in miR-22–transfected SiHa cells (Fig. 6 F). These findings indicate that miR-22 may affect the pRb pathway of cellular senescence by targeting SIRT1 and CDK6.

Lastly, we attempted to determine whether overexpression of any of the three genes could rescue the senescence phenotype in cells overexpressing miR-22. We forced SiHa or MDA-D3 cells to express SIRT1, Sp1, or CDK6 using plasmid constructs lacking 3′-UTRs of these genes. Indeed, miR-22–induced cell growth repression and SA-β-gal activity were partially rescued by the introduction of SIRT1, CDK6, or Sp1 in either SiHa cells (Fig. 6, G and H) or MDA-D3 cells (not depicted), although it seemed weak for the effect of Sp1 overexpression on cell growth, which might be because of the indirect role of Sp1 in the pRb pathway of senescence. Collectively, these findings suggest that SIRT1, Sp1, and CDK6 play an important role in miR-22–induced senescence.

miR-22 alters tumor cell morphology and suppresses cell invasiveness in vitro

Changes in cell morphology are important parameters of cancer invasion and metastasis. We performed high content analysis using Operetta to measure the morphology area of all the cells transfected with miR-22, miR-34a, or cont miR on each well of a 96-well plate (Fig. 7 A and Fig. S3 B) and analyzed cell size distribution (Fig. 7 B). We found there were significant differences in cell size distribution between miR-22–treated cells and other cells. miR-22 remarkably increased cell morphology area up to 1.6-fold overall and raised percentages of cells distributed in large cell size groups in comparison with cont miR or miR-34a, revealing that miR-22 triggers senescence morphological changes in tumor cells. In addition, miR-22–treated cells contain enhanced actin stress fibers (Fig. 7 A) similar to senescent fibroblasts, indicating that those cells are less motile (Chen et al., 2000; Belguise et al., 2005). We observed that senescent fibroblasts and Lenti-Pre22–infected cancer cells exhibiting large flattened senescence-like morphology appeared to decrease in cell movement (Fig. S4 and Videos 1–4, large GFP-positive cells), indicating that miR-22–induced senescence morphology in cancer cells could be attributed to the suppression of cell motility. Matrigel invasion assay showed that miR-22 significantly reduced the number of invaded cells in SiHa and MDA-D3 cells (Fig. 7 C), indicating that the invasive potential of cancer cells was severely affected by miR-22. Therefore, the inhibition of cancer cell invasion by miR-22 may be a result of the induction of cellular senescence.

miR-22 inhibits tumor growth and metastatic potential of aggressive breast cancer in vivo

We next asked whether miR-22 overexpression would also induce senescence in vivo and suppress tumor growth and metastasis in vivo. Using breast cancer tumor models, the cont miR–treated mice showed the apparent presence of primary tumor, whereas those injected with miR-22 complex exhibited no increase in the luminescence of primary tumor during the same observation period (Fig. 8 A, left). Judging from photon count between the cont miR– and miR-22–treated groups at the two points of the experiment, miR-22 treatment resulted in a mean decrease in tumor growth of 41.3% at day 39 ($P = 0.04$; not depicted) and 66% at day 46 ($P = 0.005$; Fig. 8 A, right), suggesting that miR-22 exerted significant tumor growth suppression in vivo. We also compared tumor metastasis with important organs in the two groups and were surprised to find that miR-22 delivery resulted in the inhibition of distant metastasis in the liver, kidney, spleen, stomach, and small intestine (Fig. 8 B). There were significant differences in the whole body of mice between the cont miR– and miR-22–treated groups on day 46 ($P = 0.004$), indicating the inhibition of metastasis by injection with miR-22 in vivo.

We also confirmed that synthetic miR-22 was delivered into primary tumor by quantitation of the miR-22 level in tumor (Fig. 8 C). Furthermore, the number of SA-β-gal–positive cells in miR-22–treated tumor dramatically increased, correlated with the amount of miR-22 in tumor (Fig. 8 D). In addition, we did not observe SA-β-gal–positive cells in nontumor cells such as vascular endothelial cells and other stroma cells of mice. Moreover, we found that the morphologies of the tumors were different; the cells in cont miR–treated groups were densely packed and slightly elongated, whereas those in miR-22–treated groups were larger and more irregularly shaped (Fig. 8 E). Pathologically, vacuolation and nuclear pyknosis associated with degradation of tumor cells were found in miR-22–treated tumor tissues. Therefore, it is possible that induction of cellular senescence in tumor cells may result in these pathological changes.

The progression toward metastasis formation requires proliferation of tumor cells at primary sites and distant sites. Notably, the expression of Ki-67 in miR-22–treated groups was significantly lower than that in cont miR–treated groups and nontreated groups (Fig. 8 F), indicating the inhibition of cell proliferation in tumor tissues treated with miR-22. Together, these findings suggest that miR-22 significantly induced cellular senescence in breast cancer in vivo, consequently inhibiting tumor growth and metastasis in vivo.

Discussion

The present study for the first time reported the functional effect of miR-22 as a novel regulator of cellular senescence in normal human and cancer cells and addressed the inhibitory role of miR-22 in tumor growth and metastasis, suggesting that miR-22–induced senescence acts as a barrier to cancer progression in vitro and in vivo. Our study extends the current understanding

activity in cont miR–transfected groups. PC, positive control. (F) Representative Western blot analysis of SIRT1, Sp1, and CDK6 in SiHa and MDA-D3 cells transfected with cont miR (C) and mature miR-22 (22) at 72 h after transfection. (G) The expression levels of SIRT1, CDK6, and pRB phosphorylation in MRC-5 and HMEC184hTERT cells were analyzed by immunoblotting. β-actin was used as a loading control and the relative density of bands was densitometrically quantified. Y, young; S, senescent; hTERT, 184hTERT. Data in all the panels represent mean ± SEM ($n = 3$). *, $P < 0.05$; **, $P < 0.01$.

Published April 18, 2011

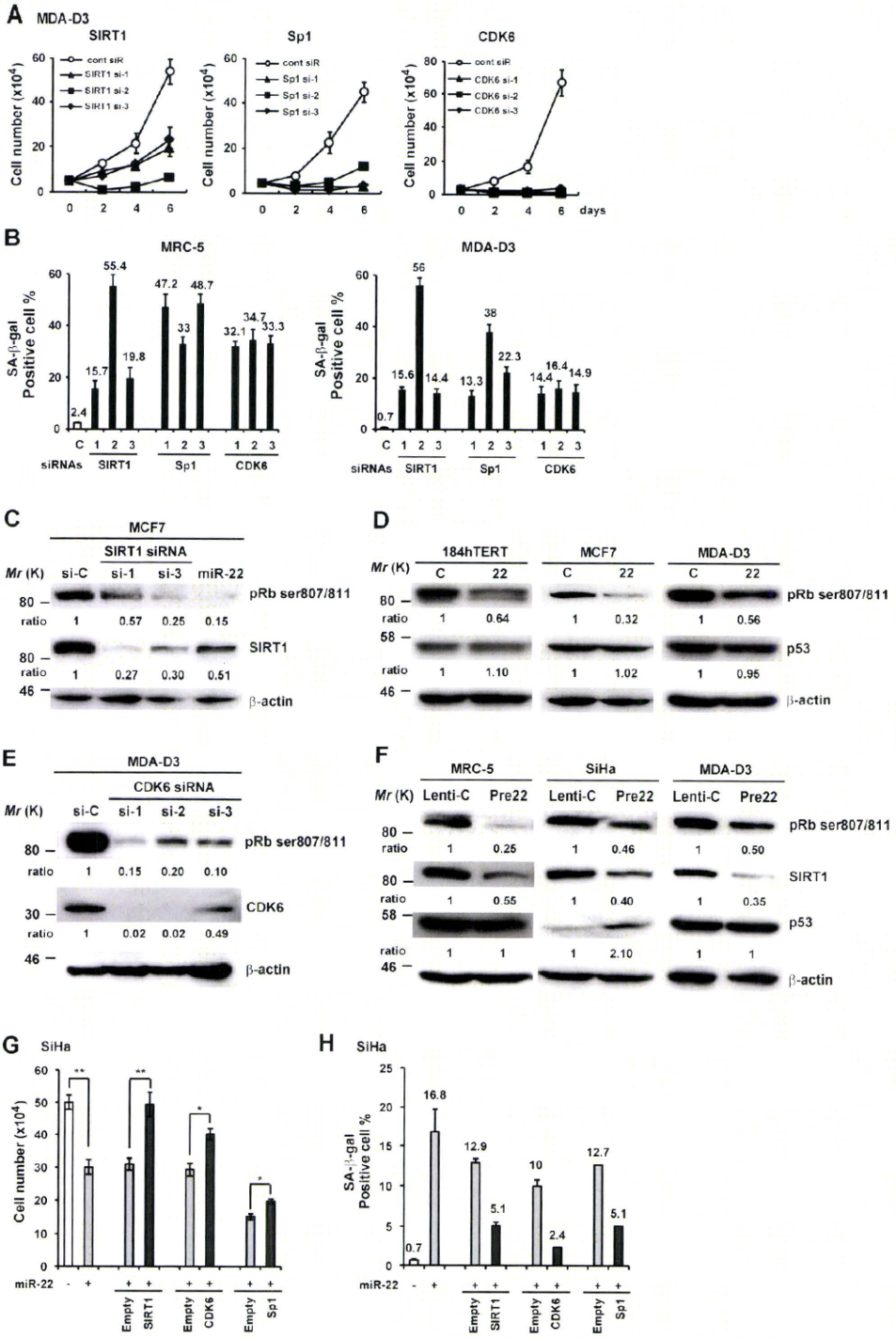

Figure 6. **SIRT1, Sp1, and CDK6 are potentially involved in miR-22–mediated cellular senescence.** (A) Representative growth curves corresponding to MDA-D3 cells transfected with cont siR or siRNAs against SIRT1, Sp1, and CDK6. Each value was determined in triplicate. (B) The histograms display the percentage of SA-β-gal–positive cells in MRC-5 and MDA-D3 cells at day 6 after siRNA transfection. (C–F) Western blot analysis was performed in those cells as indicated in each panel at 72 h after siRNA/miRNA transfection (C–E) or day 6 after infection (F). β-actin was used as a loading control and the relative density of bands was densitometrically quantified. (G and H) SiHa cells were first transfected with miR-22 duplex and, 24 h later, sequentially transfected with expressing plasmids or empty vectors as indicated. Cell proliferation (G) and SA-β-gal (H) activity was evaluated at day 6 after miRNA transfection. Data in all the panels represent mean ± SEM ($n = 3$). *, $P < 0.05$; **, $P < 0.01$.

Published April 18, 2011

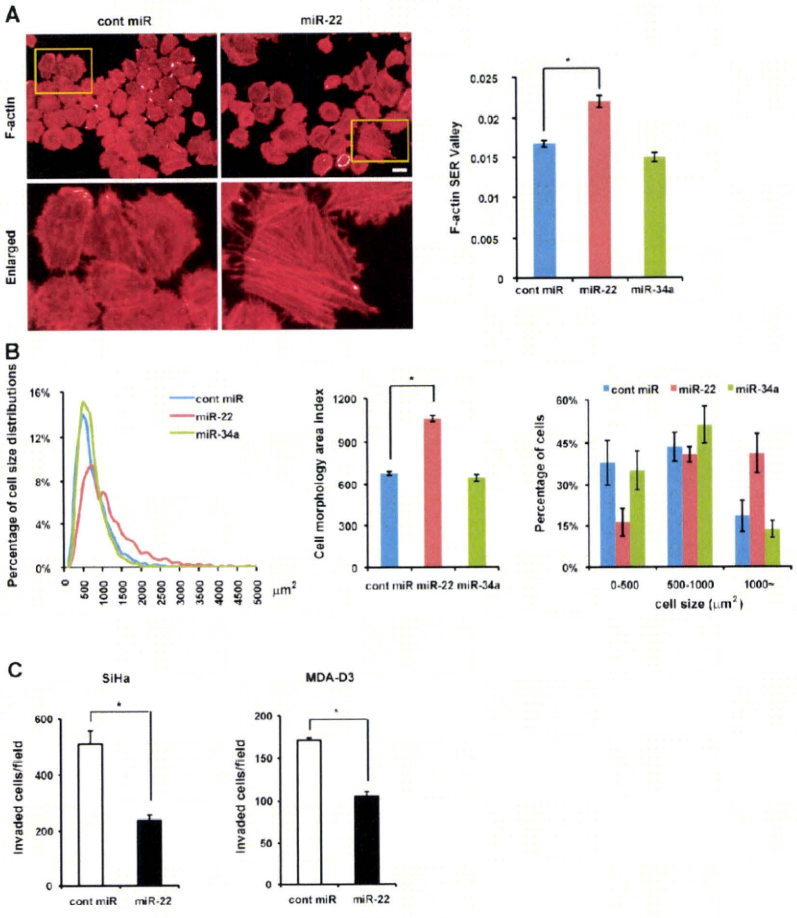

Figure 7. **Overexpression of miR-22 induces cell enlargement and inhibits cell invasion in vitro.** (A) Cell morphology area and actin stress fiber formation (stained with phalloidin) in miR-22–transfected SiHa cells were examined by confocal microscopy and compared with control cells. Enlarged images of the boxed area from the top are shown in the bottom. Bar, 20 μm (top, left and right). The histogram shows that F-actin formation was quantified using the texture analysis, and F-actin SER Valley represented occurrence of stress fiber structures within cells. (B) Cell size distribution (left), overall morphology area (middle), and percentage of cells in three groups of cell size (right) were calculated and analyzed by automated image analysis in SiHa cells. (C) Effect of miR-22 on SiHa and MDA-D3 cell invasion was measured by Matrigel invasion assay for 48 h, presented by quantitative determination of the number of invaded cells. Data in all the panels represent mean ± SEM ($n = 3$). *, $P < 0.05$.

of SA-miRNAs in tumorigenesis by unraveling the role of miR-22 in cellular senescence and tumor suppression. miRNAs present a mechanism in which genes involved in a variety of different signaling pathways can be regulated simultaneously (He and Hannon, 2004; Lafferty-Whyte et al., 2009). Not only does miR-22–induced senescence inhibit unlimited tumor cell proliferation, senescence morphological changes also suppress tumor cell motility and invasion, partially because of enhanced actin stress fibers in cancer cells, indicating that the induction of senescence contributes to the suppression of tumor cell growth, invasion, and metastasis in vitro and in vivo.

Our study shows that miR-22 is differentially expressed in normal human and cancer cells. Consistent with our results, miR-22 dysregulation in cancer and human diseases has been documented in several miRNA profiling experiments. miR-22 is down-regulated in intrahepatic cholangiocarcinoma (Kawahigashi et al., 2009) and silenced in acute lymphoblastic leukemia (Li et al., 2010) and hepatocellular carcinoma (Calin et al., 2004) but up-regulated in osteoarthritis (Iliopoulos et al., 2008). These varying levels of miR-22 expression may suggest different requirements for alterations in their target gene pathways. miR-22 regulates a repertoire of cancer-related genes; however, there is no indication of the importance of miR-22 in tumorigenesis through targeting senescence-associated genes. In the present study, gain-of-function and loss-of-function phenotypes of miR-22 demonstrated the role of miR-22 as a positive regulator of cellular senescence and identified SIRT1, Sp1, and CDK6 as critical targets of miR-22 in the senescence signaling pathway.

Previous studies have documented that SIRT1, Sp1, and CDK6 might act on the p53 and/or pRb pathway. (Ota et al., 2006; Ruas et al., 2007; Tapias et al., 2008; Brooks et al., 2009) SIRT1 plays an important role in the longevity and cellular senescence of most organisms through directly modulating the p16–pRb signaling pathway (Huang et al., 2008) as well as p53 and other proteins (Solomon et al., 2006; Brooks and Gu, 2009). The Sp1 transcription factor regulates the expression of multiple cell cycle genes, including the p53 and Sp1 gene itself (Koutsodontis et al., 2001; Tapias et al., 2008). CDK6 protein has been understood to phosphorylate pRB and delay senescence (Ruas et al., 2007; Ohtani et al., 2009). Our study demonstrated that miR-22 induced the dephosphorylation of pRB by targeting SIRT1 and CDK6. Collectively, we suppose that miR-22 regulates cellular senescence through connecting SIRT1, Sp1, and CDK6 to affect the pRb pathway and might coordinate p53 and other signaling pathways of cellular senescence in a cell type– and genetic context–dependent manner.

Published April 18, 2011

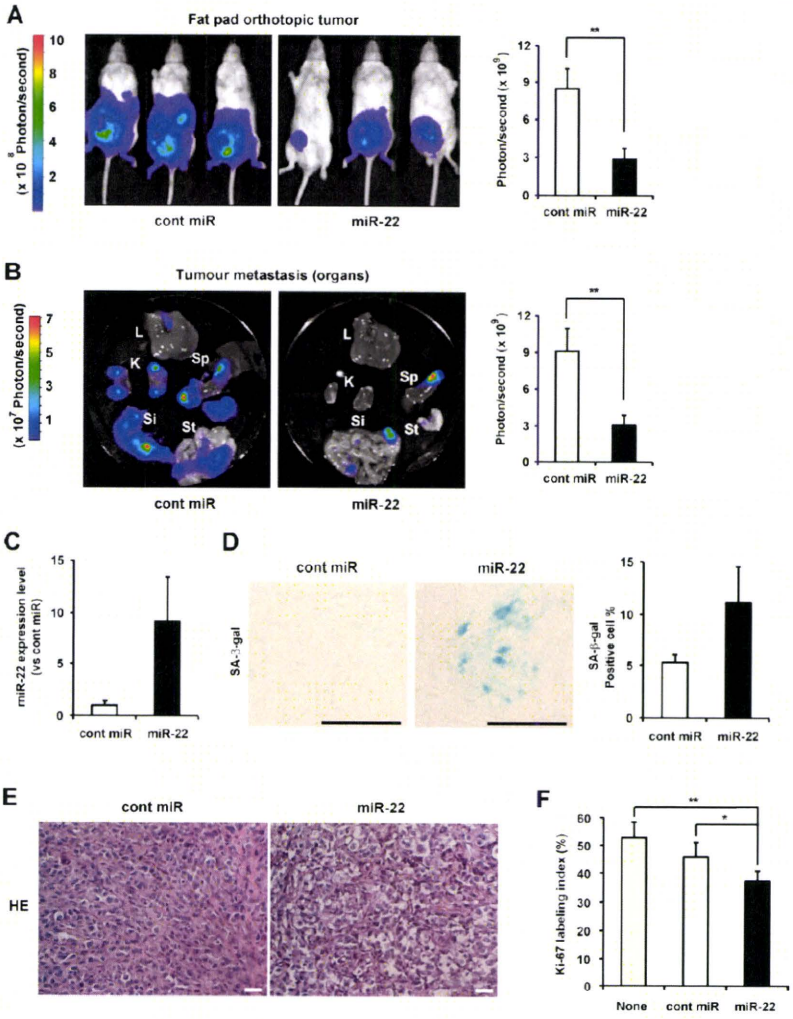

Figure 8. **Synthetic miR-22 delivery induces cellular senescence in vivo and inhibits breast tumor growth and metastasis in vivo.** (A and B) Representative fat pad orthotopic tumor (A) and selected organ (B) images of mice on day 46 after inoculation. Quantitation of bioluminescence emitted from the primary tumor (A) or whole body (B) of mice was presented as the mean ± SEM (n = 6). L, liver; K, kidney; Sp, spleen; Si, small intestine; St, stomach. (C) Relative quantitation of miR-22 level in primary tumor tissues was analyzed by qRT-PCR. Total RNA was isolated from five 10-µm-thick optimal cutting temperature compound–embedded frozen tissue sections. Expression level of miR-22 in miR-22–treated tumors was relative to that in cont miR–treated tumors set at 1. U6 was used as an internal normalization control. Data represent mean ± SEM (n = 5). (D and E) Representative histochemical detection of SA-β-gal activity in vivo (D) and hematoxylin and eosin (HE) staining (E) in primary tumor on day 46 after inoculation. Images were taken with light microscopy. Seven independent fields were chosen, and the percentage of SA-β-gal–positive cells is presented in the histogram. Data represent mean ± SEM (n = 4). Bars, 50 µm. (F) Effect of miR-22 on cell proliferation in primary tumor tissues was evaluated by Ki-67 immunostaining. The histogram displays the percentage of Ki-67 labeling index in these groups. Data represent mean ± SEM (n = 3). *, $P < 0.05$; **, $P < 0.01$.

The ability of miRNAs to affect many mRNAs is similar to the ability of transcription factors to regulate many promoters simultaneously. Recent studies demonstrate that miR-22 constitutes a feedback loop with c-myc and MYCBP and forms a regulatory loop in the phosphatase and tensin homolog–AKT pathway (Iliopoulos et al., 2008; Pandey and Picard, 2009; Bar and Dikstein, 2010; Xiong et al., 2010). The human miR-22 gene is located in a minimal loss of heterozygosity region on chromosome 17 close to p53 (Calin et al., 2004). We predict that miR-22 might induce complex changes and the extensive cooperation between miR-22 and p53 known to be involved in the senescence program, which remains to be elucidated.

miR-22 has been shown to be ubiquitously expressed in human cells and various tissues (Neely et al., 2006). Expression of miR-22 increases after the induction of stem cell differentiation and in erythropoiesis, which indicates that it might have an important role in cell development and differentiation (Choong et al., 2007; Gangaraju and Lin, 2009). miR-22 is highly expressed in mammary progenitor cells, implicating its possible role in progenitor self-renewal (Ibarra et al., 2007). To date, there is no indication of miR-22 function in normal human cells. In our study, miR-22 is particularly up-regulated upon cellular senescence in human fibroblasts and epithelial cells, and overexpression of miR-22 induced senescence phenotypes in these cells, indicating that miR-22 might emerge as the principal regulator that controls cell functions in physiological and pathophysiological settings. However, it is obscure in the mechanism that controls the increased expression of miR-22 during senescence. We attempted stable knockdown of miR-22 in early-passage MRC-5 (Fig. 2 D) and IMR90 cells (unpublished data), which resulted in both of the cells seeming younger than untreated cells. Furthermore, we investigated how stable knockdown of miR-22 affected late-passage MRC-5 cells. Our results demonstrated that those anti-22–infected presenescent MRC-5 cells appeared to be small, thin, and young with the decrease in cell morphology area and fewer SA-β-gal–positive cells (Fig. 2, C–F), indicating that inhibition of miR-22 is an obstacle for cells to undergo senescence. Given our finding that miR-22 induces cellular senescence in human fibroblasts in vitro, it will be interesting to determine whether miR-22 is involved in human aging in vivo.

Published April 18, 2011

It has been reported that the regulation of proliferation signaling, cytoskeletal remodeling, and apoptosis survival pathways would logically be required to create the senescent cell phenotype, which can be regulated by SA-miRNAs with differential timings of these complex signaling cascades (Lafferty-Whyte et al., 2009). These might give an explanation to the distinct effects of miR-22 knockdown on cell proliferation, morphology, and viability in various cells. We observed that actin stress fibers were enhanced in miR-22–transfected enlarged cells (Fig. 7 A), whereas anti-22–infected cells appeared to be small and to have fewer stress fibers (unpublished data). Moreover, we noted that cytoskeleton arrangement and focal adhesion turnover occurred with differential timing in various anti-22–infected cells and thus might affect cell growth, adhesion, and survival, which needs to be confirmed in a further study. In addition, miR-22 expression level is quite low in various cancer cells, and permanent inhibition of miR-22 induced apoptosis, indicating that miR-22 kept to a certain level seems to be essential for cellular survival. It has been reported that miR-22 targets the phosphatase and tensin homolog and anti-22 induces apoptosis in different cancer cells (Bar and Dikstein, 2010; Liu et al., 2010), which is consistent with our results.

In this study, miR-22 inhibits the proliferation of human breast cancer metastasis cell lines (MDA-D3) both in vitro and in vivo through induction of genetic reprogramming of the senescent pathway. Synthetic miR-22 injection significantly suppresses tumor growth and metastasis in a mouse model of breast cancer metastasis, indicating the therapeutic potential of miR-22 in breast cancer metastasis. Currently, the emergence of new technologies that use synthetic miRNA mimics or anti–miRNA oligonucleotides holds great promise in clinical miRNA therapy (Garofalo and Croce, 2011). The first clinical trial for LNA-antimiR-122–based hepatitis C therapeutics was initiated after the successful therapeutic application of miR-122 antagonism in mice (Elmén et al., 2008), whereas the clinical application of synthetic miRNA mimics has not been reported. Synthetic miR-22 mimic treatment in cancer will become a significant scientific and therapeutic challenge.

SA-miRNAs, such as miR-22, induce cellular senescence without causing apoptosis in cancer cells and subsequently result in tumor suppression (Fig. S5), providing a novel promising approach for the next generation of cancer therapy using nucleic acid biomedicine. We propose that permanent micromanaging of cancer cells by inducing senescence phenotypes using SA-miRNAs may be novel and efficient for protecting recurrent cancer after conventional cancer treatments without causing side effects.

Materials and methods

Cell culture

MRC-5 cells were grown in DME/F12 (1:1, vol/vol) supplemented with SAP (0.2 mM serine, 0.1 mM aspartic acid, and 1.0 mM pyruvate). MDA-MB-231-luc-D3H2LN is a luciferase-expressing cell line that was derived from MDA-MB-231 cells, maintained in RPMI1640 medium. Other human fibroblasts and cancer cells were cultured in DME. All media were supplemented with 10% FBS (vol/vol). HMEC184 cells were cultured in MEGM BulletKit (Takara Bio Inc.). TIG-3 (74–76 PDL), TIG-1 (63 PDL), TIG-114 (51 PDL), MRC-5 (58–60 PDL), and HMEC184 (22 PDL) were cultured for 2–4 wk as senescent normal cells. MRC-5 (41–51 PDL) and 184hTERT (84–100 PDL) were used as young fibroblasts and immortalized epithelial cells, respectively.

miRNA microarray

Total RNAs were harvested from young (42 PDL) and senescent (74 PDL) TIG-3 fibroblasts using the traditional acid guanidinium-phenol-chloroform extraction method and quantified with a spectrophotometer (NanoDrop; Thermo Fisher Scientific). Microarray analysis of miRNA expression was performed by both miRCURY LNA miRNA Array (Exiqon) and 3D-Gene microarray (Toray).

Real-time qPCR

Total RNA was extracted from the cells and tissues using the miRNeasy Mini kit (QIAGEN). The expression of miRNA was quantified by miRNA assays (TaqMan; Applied Biosystems). Real-time qRT-PCR was performed using a real-time PCR system (ABI StepOne and StepOnePlus; Applied Biosystems) and LightCycle 480 (Roche). Expression of miRNA was defined from the threshold cycle, and relative expression levels were calculated using the $2^{-\Delta\Delta Ct}$ method after normalization with reference to the expression of U6 small nuclear RNA.

Transient miRNA/siRNA transfection and plasmid transfection

Hsa-miR-22 duplex and negative control were obtained from QIAGEN. siRNAs targeting SIRT1, Sp1, CDK6, and negative control siRNA were purchased from Invitrogen. Cells were transfected with 10 nM of either miRNA or siRNA (except as mentioned) using Lipofectamine RNAiMax (Invitrogen) according to the manufacturer's protocol. Transfection efficiency under the conditions we adopted in this study was estimated to be >90% according to our observations made using a fluorescence-labeled double-stranded siRNA.

For rescue experiments, the expression plasmids used were pcDNA3.1-SIRT1 (a gift from B. Marshall, Gladstone Institute, San Francisco, CA), pCMVneo-CDK6 (provided by S. Van den Heuvel, Utrecht University, Utrecht, Netherlands), and CMV-Sp1 (Addgene). These constructs contain the encoding region of mRNA but lack the 3′-UTR of these genes. Cells were first transfected with miRNA in a 60-mm dish for 24 h and sequentially transfected with 0.25 µg of plasmid DNA using Lipofectamine LTX Plus reagent (Invitrogen) according to the manufacturer's protocol. The overexpression of SIRT1, Sp1, and CDK6 was confirmed by Western blotting. After a 24-h incubation, cells were seeded to 35-mm-diameter dishes and incubated for 4 d until cell proliferation assay and SA-β-gal assay.

Lentivirus infection

Lentiviruses were generated by cotransfecting 0.9 µg of lentiviral vector (premiR-22, miRZip, anti–miR-22, or empty vectors; System Biosciences) and 2.7 µg of packaging plasmid mix (1:1:1 for 0.9 µg pPACK-H1-GAG, pPACK-H1-Rev, and pVSV-G) in 293T cells using Lipofectamine LTX Plus reagent. Supernatants were collected 48 h after transfection, filtered through a 0.45-µm membrane, and directly used to infect cells. Cells were observed and images were acquired using a 10× objective with fluorescent microscopy (Axiovert 200M; Carl Zeiss) in combination with a camera (AxioCam; Carl Zeiss) and AxioVision software (Carl Zeiss) at room temperature.

Cell proliferation and SA-β-gal assay

For cell proliferation assay, 48 h after transfection or infection, 3–5 × 10^4 cells were seeded in a series of 35-mm-diameter dishes and counted for the indicated days. For cytochemical and histochemical detection of SA-β-gal activity, SA-β-gal staining was performed as described previously (Debacq-Chainiaux et al., 2009). SA-β-gal–positive cells were quantified by counting positive and negative cells at 100× magnification in at least five random independent fields. Pictures were taken with a 10× phase-contrast objective on a light microscope (IMT-2; Olympus) with a camera using Image saver (AE-6905; ATTO) at room temperature.

Automated image acquisition

SiHa cells were seeded in a 96-well Viewplate (PerkinElmer) and transfected with cont miR, miR-22, or miR-34a for 72 h. To measure cell size and F-actin, cells were fixed by 4% PFA and stained with the actin marker Rhodamine phalloidin (1:40; Invitrogen; provided by S. Kobayashi and H. Kishi, Yamaguchi University, Ube, Japan). For BrdU quantitative analysis, cells were pulse labeled with 10 µM BrdU (Sigma-Aldrich) for 1 h at 37°C, incubated with 5% CO_2, and fixed by 70% ice-cold ethanol for 30 min at room temperature. Cells were treated with 2N HCl for 20 min, neutralized with 0.2 M Tris-HCl, pH 7.5, and permeabilized with 0.1% Triton X-100 for 5 min, followed by the mouse anti-BrdU (1:200; Dako) and incubation for

Published April 18, 2011

1 h. Cells were then stained with anti–mouse AF488 (1:500; Invitrogen). DAPI (1 µg/ml; Dojindo) images were used for nuclear recognition and cell counting. Images were acquired in a fully automated and unbiased manner using a 10× objective with a spinning disk confocal microscope (Operetta; PerkinElmer) at room temperature. Eight images per well were collected to obtain a sufficient number of cells for reliable statistical analysis. Image correction and analysis were performed using custom-designed image analysis software (Harmony; PerkinElmer). The histogram in Fig. 7 A shows that F-actin was quantified using the texture analysis by Harmony software (PerkinElmer), and F-actin SER Valley represented the occurrence of stress fiber structures within cells.

FACS analysis

48 h after transfection, cells were fixed in 70% ice-cold ethanol and stained with PBS containing 50 µg/ml propidium iodide and 100 µg/ml RNase A for DNA content analysis by flow cytometry analysis on a FACSCalibur system (BD). The percentage of cells in the various cell cycle phases was calculated using ModFitLT v2.0 software (Verity Software House).

Apoptosis assays

Cells were plated in an 8-well CultureSlide (BD), and apoptotic cells were detected with traditional or modified TUNEL assay using the DeadEnd Fluorometric TUNEL System (Promega) according to the manufacturer's protocol. In modified TUNEL assay, Cy5-dUTP (GE Healthcare) was substituted for fluorescein-dUTP in a standard TUNEL reaction to detect apoptotic cells of GFP-expressed cells. Images were acquired using a 40× objective with fluorescent microscopy (Axiovert 200M) in combination with a camera (AxioCam) and AxioVision software at room temperature.

Hybridization protection assay (HPA) and Southern blot analysis

Cells were plated in a 100-mm culture dish and transfected, and DNA was extracted with a traditional phenol-chloroform 72 h after transfection. The lengths of total telomere and G-tail were determined using Southern blotting and HPA methods as described previously (Tahara et al., 2005).

Western blotting

72 h after transfection or at day 6 after infection, cells were homogenized in lysis buffer (50 mM Tris-HCl, pH 8.0, 120 mM NaCl, 1% NP-40, 100 mM NaF, 0.2 mM Na_3VO_4, and Complete mini protein inhibitor cocktail [Roche]). 30 µg of proteins in the total cell lysate was separated by SDS-PAGE and transferred to polyvinylidene fluoride membrane. Antibodies to p53 (clone BP53-12; Millipore), phospho-Rb (ser807/811; Cell Signaling Technology), and β-actin (Sigma-Aldrich) were purchased, and anti-CDK6 (C-21), SIRT1 (H-300), and Sp1 (PEP2) antibodies were purchased from Santa Cruz Biotechnology, Inc. The secondary antibodies were HRP-conjugated anti–rabbit (NA 934V) and –mouse (NA 931V) antibodies (GE Healthcare). Immunoreactive bands were visualized using an ECL Plus kit (GE Healthcare), followed by exposure to x-ray film (RX-U; Fujifilm). The density of bands was densitometrically quantified using ImageJ (National Institutes of Health).

Luciferase reporter assay

The full-length 3′-UTRs of human SIRT1 and Sp1 were amplified by PCR from genomic DNA and cloned at the SacI and XhoI sites into pmirGLO vector (Promega). The 3′-UTR fragments of human CDK6 containing three putative miR-22 binding sites were also amplified from genomic DNA and cloned at the XhoI and SalI sites into pmirGLO vector. The sense and antisense oligonucleotides for the putative miR-22 binding site at the 3′-UTR of potential targets were annealed and cloned at the SacI and XbaI sites into pmirGLO vector. An internal NotI site was added to the oligonucleotides for clone confirmation. A positive control construct contains complete complementary mature miR-22 sequence. PCR primers and oligonucleotide sequences for constructs are provided in Table S2. All the constructs were further confirmed by sequencing.

For luciferase activity analysis, each construct was cotransfected with miRNA duplex in a 96-well plate using DharmFECT Duo transfection reagent (Thermo Fisher Scientific) for 72 h, and luciferase assays were performed with the Dual-Luciferase reporter system (Promega) according to the manufacturer's instructions. Luminescent signal was quantified by luminometer (Glomax; Promega), and each value from firefly luciferase construct was normalized by Renilla luciferase assay.

Cell motility observation by fluorescence microscopy

Cells were seeded in a 4-well 35-mm dish (Greiner Bio-One) at a density of 1,000 cells/well and grown for 48 h in culture medium. Before recordings were initiated, the multidishes were left for at least 30 min on the microscope stage for temperature equilibration. Time-laspe video recordings of live cells were performed for determination of cell motility. In brief, live cells from several nonoverlapping areas were recorded in 30-min or 1-h intervals over a period of 8–24 h using a CFI Plan Apo 10× objective with a fluorescence microscope (BIOREVO BZ-9000; KEYENCE) equipped with a motorized movable microscope stage. Recordings were stored as 8-bit 680 × 512 pixel images. The microscope stage contained a thermostatically controlled heating element and was surrounded by a Plexiglas incubator, thereby ensuring that live specimens could be maintained at 37°C during recordings.

In vitro invasion assay

48 h after transfection, cells were resuspended in culture medium without serum and seeded at densities of 1.5×10^5 cells/well in 24-well Transwell inserts (8-µm pores; BD) coated with 50 µg Matrigel (BD). The lower chamber was supplemented with a medium with 10% FBS. After 48 h of incubation, the cells on the upper surface were scraped off, whereas the invasive cells attached to the lower surface of the membrane inserts were fixed and stained with hematoxylin. The invading cells were observed and counted from nine images (including at least 2,000 cells) in three fields of three membranes using a 10× phase-contrast objective under light microscopy (U-PMTVC; Olympus) at room temperature.

Tumor imaging in vivo

5-wk-old female C.B17/Icr-scid (Scid/scid) mice (CLEA Japan, Inc.) were inoculated with MDA-MB-231-luc-D3H2LN cells into the fat pad on day 0 as a 1:1 mixture of ECM gel complex and cells at 2×10^6 cells/50 µl/site. The hsa-miR-22 duplex and cont miR with RNA-jetPEI (Polyplus Transfection) complex at the ratio of 1:1 in a volume of 100 µl (20 µg/site) were injected intratumorally every other day from day 13 to 31 after inoculation. The development of subsequent tumor growth and metastasis was monitored once a week by in vivo imaging. In brief, mice were injected with 150 mg/kg D-luciferin (Promega) intraperitoneally and imaged immediately to count the photons from the whole bodies using the IVIS imaging system (Xenogen) according to the manufacturer's instructions. 10 min later, photons from firefly luciferase were counted. Data were analyzed using LivingImage software (version 2.5; Xenogen).

Immunohistochemistry

Immunohistochemical staining was performed with anti–Ki-67 monoclonal antibody (1:50; Dako) after antigen retrieval by microwave treatment in citrate buffer, pH 6.0, and detection by a streptavidin–biotin peroxidase system using the LSAB kit (Dako). The sections were incubated with primary antibody at 4°C overnight. A labeling index percentage of Ki-67 was determined by examining at least 500 tumor cells at 200× magnification in three representative and intensely stained areas using a 20× objective under light microscopy (U-PMTVC) at room temperature. The expression of Ki-67 was graded as high (>50% of positive cells) and low (<50% of positive cells).

Statistical analysis

Significance of differences between the treated samples and controls was determined by two-tailed *t* tests using Excel (Microsoft). $P < 0.05$ was considered statistically significant.

Online supplemental material

Fig. S1 shows the opposite effect of miR-22 overexpression and knockdown on apoptosis in human cancer cells. Fig. S2 shows that miR-22 has no effect on the length of total telomere or G-tail in human cancer cells. Fig. S3 shows an examination of BrdU quantity analysis, cell morphology area, and F-actin formation by automated image analysis. Fig. S4 shows the images of cell motility observation in senescent fibroblasts and Lenti-Pre22–infected MDA-D3 cells. Fig. S5 shows a scheme for the role of miR-22–induced senescence in cancer cells. Table S1 shows altered expression miRNAs identified by miRNA microarray function in cell growth and tumorigenesis. Table S2 shows PCR primers and oligonucleotide sequences for each construct of miR-22 putative targets in luciferase reporter assay. Videos 1–4 show cell motility observation of young and senescent MRC-5 cells, Lenti-C, and Lenti-Pre22–infected MDA-D3 cells, respectively. Online supplemental material is available at http://www.jcb.org/cgi/content/full/jcb.201010100/DC1.

We thank Maki Yoshida for her assistance with the invasion assay experiments, Ryo Shioda (PerkinElmer, Japan) for his technical help with automated image acquisition, Sei Kobayashi and Hiroko Kishi (Yamaguchi University) for the provided reagents, and Anno Kumiko (Hiroshima University) and Takayuki Mizutani (IZM, Inc., Japan) for their technical support.